Researches in Earth Sciences

Journal homepage: https://esrj.sbu.ac.ir

Research Article

Spatial mismatch between recorded groundwater pumping and land subsidence in the alluvial plains of Alborz province, Iran: evidence from SBAS InSAR and multitemporal LULC analysis (2010–2024)

Ariyan Allahveisi[1], Abolghasem Goorabi[1*], Mostafa Karimi[1]

1-Department of Physical Geography, Faculty of Geography, University of Tehran, Tehran, Iran

Received: 01 Aug 2026 Accepted: 04 Sep 2026

Abstract

Groundwater-related land subsidence is widespread in Iran's alluvial aquifers, yet the spatial correspondence between groundwater use, land-use/land-cover (LULC) patterns, and surface deformation remains poorly constrained. This study integrated annual Sentinel-1 SBAS-InSAR line-of-sight (LOS) deformation for 2015–2024, Random Forest LULC maps for 2010, 2015, 2020, and 2024, a provincial pumping-well inventory, and temporally resolved groundwater-monitoring records across the Tehran–Karaj, Hashtgerd, and Eshtehard plains of Alborz Province. Direct LULC–deformation comparisons were restricted to exact same-year pairs for 2015, 2020, and 2024, and spatial dependence was addressed using variograms, distance thinning, and 14-km block-level inference. Agricultural land declined by 98.99 km² (14.80%) between 2010 and 2024. Within the valid long-term InSAR footprint, 636.14 km² (19.24%) met the operational active-subsidence criterion of ≤ -20 mm yr^{-1}. Agricultural land had the most-negative mean and median annual LOS deformation in all three matched years, with Kruskal–Wallis ε^2 values of 0.378, 0.222, and 0.273. This ranking persisted in 42 of 45 spatial-thinning configurations, while the agriculture–bare-land contrast remained supported at the 14-km block scale in all three years. Static well data showed a further spatial mismatch: Tehran–Karaj contained the largest recorded pumping capacity, whereas Hashtgerd exhibited substantially more-negative long-term deformation. The recorded-discharge and subsidence-intensity centroids were separated by 15.16 km, and this distance varied only from 15.00 to 15.28 km across tested LOS thresholds. In contrast, a 23-site temporal monitoring panel showed no robust contemporaneous or 1–2-year lagged association between monitored pumping intensity and annual LOS deformation. The results indicate that groundwater-use environments are persistently associated with stronger subsidence, but recorded pumping capacity alone does not explain its spatial distribution. Hydrogeological heterogeneity and groundwater-head history are therefore critical for interpreting and managing subsidence across the three plains.

Keywords: Land subsidence, Groundwater pumping, SBAS-InSAR, Land-use/land-cover change, Spatial mismatch, Aquifer compaction, Alborz Province, Iran.

Citation: Allahveisi, A. et al, 2026. Spatial mismatch between recorded groundwater pumping and land … , *Res. Earth. Sci:* 17(3), (54-81) DOI: 10.48308/esrj.2026.107465

* Corresponding author E-mail address: goorabi@ut.ac.ir

Introduction

Land subsidence is a major geohazard in groundwater-dependent alluvial aquifers, particularly in arid and semi-arid regions where groundwater withdrawal persistently exceeds recharge (Hasan et al, 2023). Its mechanical basis is described by the effective-stress principle: groundwater-level decline reduces pore-water pressure, transfers a larger fraction of the overburden load to the sediment skeleton, and promotes compaction of compressible fine-grained layers (Galloway et al, 1999; Terzaghi, 1943). Where effective stress exceeds the preconsolidation stress, part of this compaction can become inelastic, producing permanent land-surface lowering and irreversible loss of aquifer storage capacity (Galloway et al, 1999). Because the resulting deformation can damage infrastructure, reduce drainage capacity, disrupt agricultural land, and increase susceptibility to surface fissuring, groundwater-related subsidence has become an increasingly important environmental and planning concern worldwide (Hasan et al, 2023). Iran represents an acute example of this problem. Persistent imbalance between groundwater withdrawal and natural recharge has produced widespread aquifer depletion, a condition characterized as national-scale "water bankruptcy" (Noori et al, 2021). Cumulative depletion of non-renewable groundwater reserves was estimated at approximately 133 billion m³ between 1965 and 2019, while observation-well analyses indicate substantial long-term groundwater-storage losses across the country (Noori et al, 2021; Safdari et al, 2022). National-scale InSAR analyses further indicate that more than 31,400 km² of Iran is subsiding at rates exceeding 10 mm yr^{-1}, with substantially higher rates in critically stressed agricultural aquifers (Payne et al, 2025). The Central Plateau, including the Tehran–Alborz region, is among the areas most strongly affected by groundwater depletion and associated deformation (Safdari et al, 2022). Land-use/land-cover (LULC) patterns provide an important spatial context for interpreting this deformation, but they should not be treated as direct proxies for aquifer compaction. Agricultural and urban land constitute a large proportion of globally mapped subsiding areas (Hasan et al, 2023). In irrigated agricultural systems, expansion or intensification can increase groundwater demand and thereby contribute to hydraulic-head decline, whereas urbanization can alter recharge through surface sealing and, in some settings, add static loading to compressible sediments (Liu et al, 2023; Zhao et al, 2024). Conversely, conversion of cropland to bare or abandoned land may itself reflect prolonged water scarcity, soil degradation, or declining agricultural viability. Such transitions have been documented in Alborz Province (Goorabi et al, 2025; Nakhaei et al, 2023). LULC and deformation should therefore be interpreted as components of a coupled human–environmental system in which water demand, recharge, land management, climate, and aquifer properties interact rather than as a simple one-way causal relationship. Multitemporal InSAR provides a particularly suitable basis for examining these interactions because it can resolve spatially extensive deformation over long observation periods. Conventional differential InSAR can be affected by atmospheric delay and temporal or spatial decorrelation, whereas Persistent Scatterer Interferometry performs best where stable point reflectors are abundant (Ferretti et al, 2001). The Small Baseline Subset (SBAS) approach reduces temporal and perpendicular baselines between interferometric pairs and can therefore provide broader spatial coverage over extensive agricultural and alluvial surfaces (Berardino et al, 2002; Liu et al, 2023). In parallel, multitemporal optical and radar imagery combined with machine-learning classifiers such as Random Forest enables reproducible mapping of LULC dynamics (Asghari Saraskanrood et al, 2025; Liu et al, 2023; Norouzi et al, 2025). A major inferential challenge, however, is that dense InSAR observations are spatially autocorrelated and cannot be treated as thousands of independent samples. Effect sizes and explicit spatial-sensitivity procedures are therefore required to avoid overconfident inference based solely on nominal pixel-level significance. Previous studies in Alborz Province demonstrate both the severity of subsidence and the hydrogeological variability of its three principal alluvial plains. In Hashtgerd, SBAS time-series analysis has documented substantial deformation together with a relationship between subsidence and groundwater-level decline (Rostami et al, 2023), while Sentinel-1 observations for 2014–2023 indicate cumulative subsidence exceeding 90 cm in parts of the plain (Kalantarian et al, 2025). Hazard-zonation studies have also identified groundwater abstraction and geological conditions among the principal factors associated with subsidence susceptibility in Hashtgerd (Mehrnoor et al, 2023). In the Tehran–Karaj Plain, maximum deformation rates of approximately 158 mm yr^{-1} have been reported, together with an approximately two-year lag between groundwater-level decline and peak surface deformation, consistent with delayed consolidation of compressible layers (Shiri et al, 2024). Eshtehard and adjacent western sectors of Alborz Province have likewise experienced substantial deformation and surface fissuring (Kalantarian et al, 2025; Norouzi et al, 2025; Ghanbari et al, 2026). Collectively, these studies establish groundwater-related compaction as an important regional process while also indicating that the magnitude and timing of surface response vary spatially among the plains. Three gaps remain particularly relevant to an integrated analysis of this region. First, much of the existing evidence concerns individual plains or hazard assessments conducted under different analytical frameworks, limiting quantitative comparison among Tehran–Karaj, Hashtgerd, and Eshtehard using common spatial and statistical criteria. Second, LULC has generally been treated as a static explanatory or hazard-zonation factor; temporally matched comparisons between LULC class and deformation at multiple epochs, with explicit treatment of spatial dependence, remain limited. Third, spatial and temporal groundwater evidence have rarely been separated analytically. Conceptual spatial decoupling between pumping and subsidence has been recognized in parts of the region (Kalantarian et al, 2025), but the regional magnitude and robustness of this mismatch remain insufficiently quantified. Likewise, the approximately two-year response reported between groundwater level and deformation in Tehran–Karaj (Shiri et al, 2024) does not establish that recorded pumping intensity itself exhibits the same lag. Distinguishing static spatial correspondence from within-site temporal association is therefore necessary to avoid conflating groundwater-use location, pumping variability, hydraulic-head response, and surface deformation. To address these gaps, this study integrates annual descending-orbit Sentinel-1 SBAS-InSAR line-of-sight (LOS) deformation for 2015–2024 with LULC maps for 2010, 2015, 2020, and 2024, a static pumping-well inventory, and temporally resolved groundwater-monitoring records across the Tehran–Karaj, Hashtgerd, and Eshtehard alluvial plains of Alborz Province. The 2010 LULC map is used as a baseline for land-cover change, whereas direct LULC–deformation comparisons use temporally matched observations from 2015, 2020, and 2024.

Four research questions guide the analysis:

1) What are the spatial pattern and long-term severity of LOS deformation across the three-plain analysis region during 2015–2024?

2) How did LULC change between 2010 and 2024, and do same-year deformation distributions differ among LULC classes in 2015, 2020, and 2024 after accounting for spatial dependence?

3) How does the spatial distribution of recorded pumping capacity and groundwater-use type correspond to long-term deformation, and how robust is the resulting pumping–subsidence centroid mismatch to the operational deformation threshold?

4) Do within-site variations in monitoring-based pumping intensity show reproducible contemporaneous, one-year, or two-year associations with annual LOS deformation?The study contributes to regional subsidence research in four complementary ways. First, it evaluates the three principal alluvial plains within a common deformation and spatial-analysis framework. Second, it replaces temporally mismatched LULC–deformation comparisons with same-year pairings and evaluates their robustness using effect sizes, spatial thinning, and block-level inference. Third, it treats the static well inventory and temporally resolved monitoring records as analytically distinct groundwater datasets, thereby separating spatial co-location from temporal pumping–deformation association. Fourth, it quantifies the spatial mismatch between recorded pumping capacity and long-term deformation intensity and evaluates its sensitivity to the operational subsidence threshold.

This structure allows spatial association, temporal association, and causal interpretation to remain explicitly distinguished throughout the analysis.

Materials and Methods

Study Area

Alborz Province is situated on the southern flank of the central Alborz Mountains, immediately west of metropolitan Tehran, and covers approximately 5,182 km² (Alborz Plan and Budget Organization, 2024). The province exhibits a pronounced north–south physiographic transition from mountainous bedrock terrain to Quaternary alluvial fans and plains. This study focuses on the three principal groundwater-dependent alluvial plains of the southern sector: Tehran–Karaj, Hashtgerd, and Eshtehard (Fig. 1). The mountainous Taleghan sector was excluded from quantitative analysis because it is dominated by steep, resistant bedrock terrain with limited compressible alluvium and negligible deformation relative to the southern plains (Agha alikhani et al, 2021; Goorabi et al, 2025). The quantitative analysis domain comprised the six counties of Karaj, Fardis, Chaharbagh, Savojbolagh, Nazarabad, and Eshtehard, with an exact vector-union area of 4,079.1 km². Although the LULC classifications were generated within the wider provincial processing context to preserve spectral representation, all quantitative results reported in this study—including LULC class areas and changes, same-year LULC–deformation comparisons, statistical tests, well-based analyses, and centroid calculations—were evaluated within this common six-county domain. Minor differences between the vector area and raster-based valid areas arise from the common 30 m grid and finite-data masks and are reported where relevant.

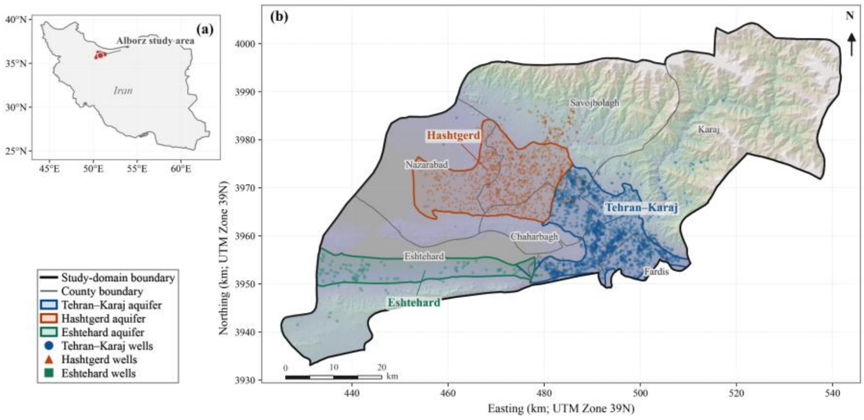

Fig. 1: Location of Alborz Province and the three alluvial plains included in the quantitative analysis.

The three plains share a groundwater-dependent, multilayered Quaternary alluvial setting but differ in recharge conditions and sediment architecture. The northern piedmont zones are generally dominated by coarser, more permeable alluvial-fan deposits, whereas the central and southern parts contain progressively finer silt- and clay-rich interbeds that are more susceptible to compaction (Kalantarian et al, 2025; Shiri et al, 2024). The regional climate becomes increasingly arid toward the southern plains, with potential evaporation greatly exceeding precipitation. Tehran–Karaj receives substantial surface-water input from the Karaj River, whereas Hashtgerd relies more strongly on the smaller Kordan River; Eshtehard represents the driest of the three systems (Ghanbari, 2026; Nakhaei et al, 2023). These contrasts in recharge opportunity and compressible sediment distribution provide the hydrogeological context for evaluating spatial differences in groundwater-related deformation without assuming that identical recorded pumping pressure produces an identical surface response among the three plains.

Analytical Workflow

The analytical framework comprised six linked stages integrating remote sensing, InSAR deformation, groundwater records, and spatially explicit statistical analysis (Fig. 2). Google Earth Engine (GEE) was used for optical and radar-image preprocessing, predictor construction, Random Forest LULC classification, and LULC change analysis; the Sentinel-1 SBAS deformation time series was generated independently in ENVI/SARscape; and the subsequent statistical, spatial-autocorrelation, groundwater, and centroid analyses were performed using the Python scientific-computing environment. In the first stage, the principal input datasets were prepared and harmonized: Landsat-5 TM, Landsat-8 OLI, Sentinel-2 optical imagery, Sentinel-1 GRD backscatter used as an LULC predictor, the SRTM DEM, annual Sentinel-1 SBAS LOS deformation for 2015–2024, the static pumping-well inventory, and temporally resolved groundwater-monitoring records. In the second stage, six-class LULC maps were produced for 2010, 2015, 2020, and 2024 using epoch-specific Random Forest models, followed by change detection and transition analysis for 2010–2015, 2015–2020, and 2020–2024. The 2010 map served only as the baseline for LULC change because it predates the available InSAR record.

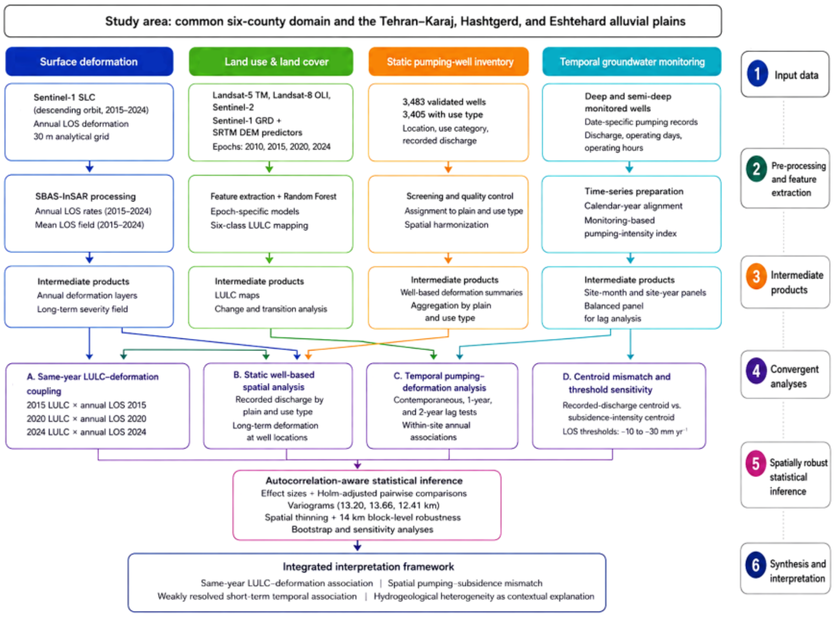

Fig. 2: Analytical workflow of the study. Four complementary data streams—multitemporal land-use/land-cover observations, Sentinel-1-derived surface-deformation data, a static pumping-well inventory, and temporally resolved groundwater-monitoring records—were integrated through six sequential stages: input-data assembly, preprocessing and feature extraction, generation of intermediate products, convergent analyses, spatially robust statistical inference, and integrated interpretation. The 2010 LULC map served exclusively as the change-detection baseline, whereas direct LULC–deformation comparisons used exact same-year pairs for 2015, 2020, and 2024. Annual LOS deformation fields were used for temporally matched LULC analyses, while the 2015–2024 mean LOS field supported long-term severity mapping, static well-based spatial analysis, and centroid-mismatch assessment. Statistical inference incorporated effect sizes, Holm-adjusted pairwise comparisons, variogram-based assessment of spatial dependence, spatial thinning, 14-km block-level robustness, bootstrap analysis, and threshold-sensitivity tests. The final synthesis explicitly distinguished spatial groundwater-pumping–subsidence mismatch from within-site short-term temporal pumping–deformation association.

The third stage characterized the deformation field. Annual LOS rates for 2015–2024 were used to describe temporal deformation, whereas the 2015–2024 mean LOS field was used for long-term severity zonation, well-based spatial summaries, and centroid analysis. In the fourth stage, direct LULC–deformation coupling was restricted to exact same-year pairs: 2015 LULC with annual LOS deformation in 2015, 2020 LULC with annual LOS deformation in 2020, and 2024 LULC with annual LOS deformation in 2024. Open-water pixels were excluded from these comparisons because persistent water surfaces do not provide reliable interferometric phase information. Class-level differences were evaluated using nonparametric effect-size and pairwise procedures, with empirical variograms, spatial thinning, and block-level analysis used to assess robustness to spatial autocorrelation. In the fifth stage, the two groundwater datasets were analyzed separately according to the information they contain. The static well inventory was used to evaluate the spatial distributions of recorded operational discharge, groundwater-use categories, plain-level pumping capacity, and long-term deformation at well locations. The temporally resolved monitoring dataset was used independently to test whether within-site variation in the monitoring-based pumping-intensity index was associated with annual LOS deformation contemporaneously or at lags of one and two years. In the sixth stage, the spatial correspondence between recorded pumping capacity and long-term subsidence intensity was quantified using weighted centroids, and the sensitivity of centroid separation and active-subsidence extent to operational LOS thresholds was evaluated before the LULC, groundwater, temporal, and spatial-mismatch evidence was synthesized. All quantitative outputs reported in the study were evaluated within the common six-county analysis domain. Spatial datasets used for cross-layer analyses were referenced to EPSG:32639 (WGS 84 / UTM zone 39N) and harmonized to a common 30 m analytical grid using source-appropriate resampling or aggregation procedures described in the following subsections. This common spatial framework ensured that LULC area estimates, same-year deformation comparisons, spatial-autocorrelation analyses, well-based summaries, and centroid calculations were evaluated over explicitly defined and comparable spatial supports.

Data

Remote-Sensing Data

The remote-sensing data consisted of two analytically distinct Sentinel-1 streams together with multitemporal optical imagery and topographic data (Table 1). LULC classification used Landsat-5 TM Collection 2 Level-2 surface reflectance for 2010, Landsat-8 OLI Collection 2 Level-2 surface reflectance for 2015 (Roy et al., 2014), and Sentinel-2 surface reflectance for 2020 and 2024. Sentinel-1 GRD imagery acquired in Interferometric Wide (IW) mode with VV and VH polarizations was used only as a continuous radar predictor for the 2015, 2020, and 2024 LULC classifications. Both ascending- and descending-orbit GRD observations were retained to improve spatial coverage. This GRD predictor stream was entirely separate from the descending-orbit Sentinel-1 SLC dataset used for SBAS deformation processing. The latter comprised the 2015–2024 interferometric archive from which 147 acquisitions were retained after SBAS network and quality-control screening; the interferometric selection and processing criteria are described separately in the Subsidence-Rate Data and Severity Zonation subsection. The 30 m SRTM DEM supplied elevation and the derived slope, aspect, and topographic position index (TPI) predictors. To maximize seasonal comparability among LULC epochs, optical composites were constructed from observations within the March–September growing-season window after scene-level and pixel-level quality screening. The retained optical support consisted of seven Landsat-5 observations for 2010 (26 May–7 August), 18 Landsat-8 observations for 2015 (6 April–29 September), 100 Sentinel-2 observations for 2020 (6 March–27 September), and 100 Sentinel-2 observations for 2024 (12 March–26 September). Corresponding Sentinel-1 GRD predictor composites used three observations in 2015 (6–11 April), 142 observations in 2020 (2 March–30 September), and 105 observations in 2024 (1 March–27 September). Thus, the final 2024 LULC epoch represents the same March–September seasonal framework used for the earlier classifications and is not based on an incomplete subsequent-year growing season. All cross-layer analyses were conducted in EPSG: 32639 on a common 30 m analytical grid. Landsat and SRTM inputs were already available at 30 m; continuous Sentinel-2 spectral and red-edge layers were resampled to 30 m using bilinear interpolation, while the Sentinel-1 GRD-derived continuous predictor layers were evaluated on the same 30 m analysis grid. Detailed sensor-specific masking, compositing, harmonization, and feature construction procedures are provided below.

Table 1: Remote-sensing datasets, temporal support, spatial resolution, and analytical roles used in the study.

Dataset / product	Source/native spatial resolution	Retained temporal support	Common analytical resolution	Role in analysis
Landsat-5 TM Collection 2 Level-2 SR	30 m	2010: 7 observations, 26 May–7 Aug	30 m	Optical predictors for 2010 LULC
Landsat-8 OLI Collection 2 Level-2 SR	30 m	2015: 18 observations, 6 Apr–29 Sep	30 m	Optical predictors for 2015 LULC
Sentinel-2 SR	10–20 m for selected spectral/red-edge bands	2020: 100 observations, 6 Mar–27 Sep; 2024: 100 observations, 12 Mar–26 Sep	30 m	Optical and red-edge predictors for 2020 and 2024 LULC

Sentinel-1 GRD, IW, VV/VH	10 m pixel spacing	2015: 3 observations, 6–11 Apr; 2020: 142 observations, 2 Mar–30 Sep; 2024: 105 observations, 1 Mar–27 Sep	30 m	Continuous C-band VV/VH and VH/VV predictors for LULC; ascending + descending coverage
Sentinel-1 SLC, VV, descending orbit	Native SLC SAR geometry	2015–2024; 147 acquisitions retained after SBAS quality control	30 m deformation products	Independent SBAS-InSAR LOS deformation time series
SRTM DEM	30 m	Static	30 m	Elevation, slope, aspect, and TPI

Note: SR = surface reflectance; GRD = Ground Range Detected; SLC = Single Look Complex; IW = Interferometric Wide swath; TPI = topographic position index. The Sentinel-1 GRD and SLC datasets served different purposes and were processed independently: GRD backscatter was used only as an LULC predictor, whereas descending-orbit SLC acquisitions supported SBAS-InSAR deformation estimation. All quantitative cross-layer analyses were performed on the common 30 m grid in EPSG: 32639.

Field and Ancillary Data

Groundwater information was obtained from two analytically distinct provincial datasets and was kept separate throughout the analysis. The first was the static pumping-well inventory supplied by the Alborz Regional Water Company. Following the initial database screening, the inventory contained 3,483 validated well records with spatial coordinates and associated groundwater attributes. The principal fields used in this study were recorded operational discharge (L s^{-1}), groundwater-use category, and alluvial-plain assignment. Recorded discharge was treated as an administrative measure of reported operating capacity rather than as measured annual abstraction, because the inventory did not provide a temporally complete series of realized pumping volumes or operating durations for individual wells. The inventory was therefore used only for spatial analyses of pumping capacity, groundwater-use category, deformation at well locations, and weighted centroids. The Alborz Regional Water Company also provided the hydrogeological technical reports used for contextual interpretation of the three plains. The static inventory underwent additional analysis-specific quality control after spatial harmonization. Wells were checked for valid coordinates, assigned to the common analysis geometry, and linked to the 30 m 2015–2024 mean LOS deformation field in EPSG: 32639. Of the source inventory, 3,407 records fell within the six-county analysis domain and 3,405 had a valid long-term deformation value and a recorded use category; these 3,405 wells formed the use-based aggregation. Of these, 3,087 were assigned specifically to the Tehran–Karaj, Hashtgerd, or Eshtehard alluvial plains and formed the three-plain aggregation. The global discharge-weighted centroid used a still more restrictive subset of 3,061 wells within those three plains that had valid coordinates and positive recorded operational discharge. These populations were kept distinct because filtering by analysis domain, deformation support, plain assignment, use category, and positive discharge serves different analytical purposes; totals derived from one subset were not treated as interchangeable with those from another. The well-to-deformation linkage used the value of the common 30 m long-term LOS field at each well location. The second groundwater dataset was a temporally resolved provincial monitoring workbook containing 18,414 measurement records. The database included UTM coordinates, Persian-calendar observation dates, source type, plain, groundwater use, discharge (debi, L s^{-1}), daily operating duration (saat, h day^{-1}), number of operating days during the month (tedad), measurement method, and status or explanatory fields for missing observations. Its full temporal coverage extended from Persian year 1381 to 1402; after conversion of valid records to Gregorian dates, observations ranged from 23 September 2002 to 16 March 2024. Site identity was defined by unique UTM-coordinate pairs. For the pumping–deformation lag analysis, the dataset was restricted to deep and semi-deep wells in the Tehran–Karaj, Hashtgerd, and Eshtehard plains, yielding 11,792 records from 82 monitoring sites. Qanats, springs, records assigned outside the three target plains, and other source types were excluded from the primary lag analysis. Quality control of the temporal records was performed before temporal aggregation. Monthly pumping volume was estimated only when discharge, daily operating hours, and monthly operating days were all available and physically plausible, using $V\_m = Q \times H \times D \times 3.6$, where Q is discharge in L s^{-1}, H is operating time in h day^{-1}, and D is the number of operating days in the month, giving V_m in m^3 $month^{-1}$. Records with incomplete pumping triplets remained missing; status annotations such as inactive or dry were not automatically converted to zero pumping. Values outside physically admissible operating-hour or operating-day limits were excluded. Where more than one observation occurred for the same site and calendar month, the median valid monthly value was retained rather than summing repeated visits. Because monthly coverage was incomplete and heterogeneous among sites and years, observed monthly volumes were not summed and interpreted as complete annual abstraction. Instead, the median observed monthly pumping volume for each site-year was used as a monitoring-based pumping-intensity index. The primary temporal analysis was restricted to 2015–2023 because monitoring coverage in 2024 ended in March and was therefore incomplete for annual comparison. A balanced-panel criterion required at least three valid pumping months in every year from 2015 through 2023. This produced 23 monitoring sites—9 in Tehran–Karaj, 10 in Hashtgerd, and 4 in Eshtehard—which formed the primary sample for the contemporaneous, one-year, and two-year lag analyses. Alternative coverage thresholds were retained for sensitivity testing. The monitoring-based pumping-intensity index is therefore an observation-based measure of temporal pumping pressure at monitored sites and should not be interpreted as total annual groundwater abstraction from any individual plain or from the regional aquifer system. Ancillary hydrogeological and climatic information used to interpret differences among the three plains was compiled from the provincial technical reports and published sources cited in the Study Area and Discussion sections. These contextual datasets informed interpretation of recharge conditions, aquifer architecture, and sediment characteristics but were not entered as measured explanatory covariates in the principal statistical models. Consequently, the quantitative analyses distinguish directly observed deformation, LULC, well-capacity, and monitoring data from hydrogeological mechanisms proposed as contextual explanations.

Subsidence-Rate Data and Severity Zonation

Annual ground-deformation fields were derived from a descending-orbit Sentinel-1 C-band SLC archive processed using the Small Baseline Subset (SBAS) approach in ENVI/SARscape. The interferometric processing was performed independently of Google Earth Engine, and the resulting annual line-of-sight (LOS) deformation products for 2015–2024 were subsequently represented on the common 30 m analytical grid in EPSG: 32639 for integration with the other spatial datasets. The SBAS acquisition strategy targeted approximately monthly temporal sampling. Candidate interferometric connections were constrained to maximum temporal and perpendicular baselines of 36 days and 60 m, respectively. Following network construction, connections with coherence values below 0.555 were excluded during quality-control screening. The final connected SBAS dataset retained 147 descending-orbit VV-polarized Sentinel-1 acquisitions for phase unwrapping and time-series inversion. Topographic phase was removed using the 30 m SRTM DEM. No dedicated atmospheric-phase-screen correction was applied. Instead, acquisitions were screened before interferometric processing and excluded when acquisition conditions were considered unfavorable, principally during periods of substantial precipitation or pronounced short-term atmospheric water-vapor variability that could introduce spatially heterogeneous tropospheric delay. The deformation time series was referenced to a stable bedrock outcrop bordering the alluvial plains. Because only a single descending viewing geometry was available, the resulting measurements represent LOS motion rather than independently resolved vertical displacement. Negative LOS values denote motion away from the satellite and are interpreted here as the subsidence-dominated component of the deformation field; positive LOS values denote motion toward the satellite and are not interpreted automatically as vertical uplift. Residual atmospheric, reference-point, phase-unwrapping, and viewing-geometry uncertainties are considered explicitly in the Limitations and Uncertainties section. Two temporal representations of the deformation data were used for different analytical purposes. Annual LOS fields were retained for 2015–2024 to describe temporal deformation and to support the exact same-year LULC comparisons. Specifically, the 2015, 2020, and 2024 LULC maps were paired only with the annual LOS deformation fields from 2015, 2020, and 2024, respectively. The 2010 LULC epoch was not coupled with deformation because it predates the Sentinel-1 SBAS record. Separately, the 2015–2024 mean LOS-rate field was used as the long-term deformation indicator for severity zonation, deformation summaries at static well locations, and spatial-centroid analyses. No multiyear deformation window was substituted for the annual field in the same-year LULC comparisons. A study-specific operational threshold of −20 mm yr⁻¹ was used to distinguish the more strongly negative portion of the long-term LOS field for subsidence-severity screening. This threshold is not treated as a formal sensor detection limit, a universal InSAR uncertainty bound, or an engineering-damage threshold. Rather, it provides a consistent operational criterion for separating stronger negative LOS deformation from the near-zero and weak-deformation portion of the regional distribution while preserving a reproducible basis for spatial zonation. Pixels with finite 2015–2024 mean LOS rates greater than −20 mm yr⁻¹ were assigned to the stable/low-deformation class for the purposes of this regional screening analysis, whereas pixels with rates ≤ −20 mm yr⁻¹ were treated as active-subsidence pixels. All severity calculations were restricted to finite InSAR observations within the exact six-county analysis mask; areas without valid long-term InSAR support were retained as NoData and were not classified as stable. The sensitivity of conclusions to the operational threshold was evaluated explicitly by repeating the active-subsidence and centroid calculations at −10, −15, −20, −25, and −30 mm yr⁻¹. For each threshold, active-subsidence extent and the subsidence-intensity-weighted centroid were calculated using identical spatial-support and weighting rules. The −20 mm yr⁻¹ criterion was retained as the primary threshold, whereas the surrounding thresholds quantify how strongly the mapped active area and the centroid-based spatial-mismatch metric depend on this analytical choice. The resulting sensitivity statistics are reported in the Results and Discussion section rather than being incorporated into the definition of the primary threshold. For descriptive severity zonation of the 2015–2024 mean LOS field, active deformation was subdivided using the empirical class boundaries adopted in the study: slight (−40 < LOS rate ≤ −20 mm yr⁻¹), moderate (−120 < LOS rate ≤ −40 mm yr⁻¹), severe (−225 < LOS rate ≤ −120 mm yr⁻¹), and critical (LOS rate ≤ −225 mm yr⁻¹), together with the stable/low-deformation class (> −20 mm yr⁻¹). These internal boundaries originated from the Jenks natural-breaks classification framework (Jenks, 1967) applied to the deformation distributions and are used only to describe relative regional deformation severity. They should not be interpreted as validated structural-damage thresholds or as probability-based hazard classes.

LULC Classification

Design and Preprocessing

Six LULC classes were mapped consistently across all four epochs: urban, agriculture, bare land, rangeland, vegetation, and water. Because sensor availability differed among years, each epoch was classified with a separately trained Random Forest model using the predictors available for that epoch; no fitted classifier was transferred between years. The 2010 model used Landsat-5 optical predictors, spectral indices, and topographic variables. The 2015 model additionally incorporated Sentinel-1 GRD radar predictors, while the 2020 and 2024 Sentinel-2 models also incorporated red-edge information. Image loading, training-sample management, and classification were performed within the wider provincial processing domain to preserve the full reference set and spectral variability, whereas all quantitative LULC areas, changes, and LULC–deformation analyses reported in this study were evaluated within the common six-county analysis domain. Optical preprocessing followed a common seasonal framework for the four epochs. Candidate Landsat and Sentinel-2 scenes were restricted to the March–September growing season and to scene-level cloud fractions below 20%. Landsat-5 and Landsat-8 Collection-2 Level-2 observations were screened using the QA_PIXEL band to remove cloud, cloud-shadow, and dilated-cloud pixels before application of the Collection-2 surface-reflectance scaling factors. Sentinel-2 observations were screened using the Scene Classification Layer, excluding cloud shadow, medium- and high-probability cloud, and cirrus classes. After pixel-level masking, the retained observations for each epoch were reduced to median composites to limit the influence of residual cloud contamination and anomalous observations. The exact retained temporal support for each sensor and epoch is reported in Table 1. Cross-sensor optical predictors were harmonized to six common spectral channels: blue, green, red, near-infrared (NIR), shortwave-infrared 1 (SWIR1), and shortwave-infrared 2 (SWIR2). Sentinel-2 continuous spectral layers were resampled using bilinear interpolation for integration on the common 30 m analytical grid. The original Sentinel-2 red-edge bands required for the 2020 and 2024 feature stacks were retained separately before feature assembly. SRTM elevation was referenced to the same EPSG: 32639 grid before derivation of the topographic predictors. Sentinel-1 GRD preprocessing and the construction of spectral, radar, red-edge, and topographic features are described in the following subsection.

Spectral Indices and Auxiliary Features

Five derived spectral indices were calculated from the harmonized optical bands for every LULC epoch (Table 2): the Normalized Difference Vegetation Index (NDVI) to characterize vegetation greenness, the Modified Normalized Difference Water Index (MNDWI) to enhance open-water surfaces, the Normalized Difference Built-up Index (NDBI) to emphasize built-up characteristics, the Bare Soil Index (BSI) to improve discrimination of exposed soil and bare land, and the Enhanced Vegetation Index (EVI) to provide complementary sensitivity to denser vegetation (Huete et al., 2002; Rikimaru et al., 2002; Tucker, 1979; Xu, 2006; Zha et al., 2003). For the Sentinel-2 epochs of 2020 and 2024, four additional red-edge bands—B5, B6, B7, and B8A—were retained as direct predictors, and the Normalized Difference Red-Edge Index (NDRE) was calculated as (B8A − B5)/(B8A + B5) to provide additional information on canopy chlorophyll and vegetation condition (Delegido et al, 2011). Sentinel-1 GRD supplied three radar predictors for the 2015, 2020, and 2024 classifiers: VV backscatter, VH backscatter, and the polarization-ratio predictor expressed in decibel space as VH_dB−VV_dB, which is equivalent to the logarithmic VH/VV ratio. The COPERNICUS/S1_GRD observations were used in their decibel representation rather than being converted from linear power. VV and VH were spatially smoothed before median compositing, and low-backscatter edge noise was screened before feature assembly. Both ascending- and descending-orbit observations were combined for this LULC predictor stream; these radar predictors were independent of the descending-orbit Sentinel-1 SLC data used for SBAS-InSAR deformation estimation. Four topographic predictors were included in every epoch-specific classifier: elevation, slope, aspect, and topographic position index (TPI). Elevation was obtained from the 30 m SRTM DEM, slope and aspect were derived from the same projected DEM, and TPI was calculated as the difference between each DEM pixel and the mean elevation within a 300 m neighborhood. These variables were included to represent broad physiographic controls on the spatial distribution of LULC classes rather than as causal predictors of land-cover change. The final predictor stacks therefore contained 15 variables in 2010 (six optical bands, five spectral indices, and four topographic variables), 18 variables in 2015 (the 2010-type predictor structure plus three Sentinel-1 radar variables), and 23 variables in both 2020 and 2024 (six optical bands, five spectral indices, four topographic variables, three radar variables, and five Sentinel-2 red-edge predictors).

Table 2: Derived spectral and radar indices and auxiliary predictors used in the epoch-specific LULC classifications.

Predictor / group	Formula or source variable	Primary information represented	Epochs used	Reference
NDVI	$\frac{(NIR - Red)}{(NIR + Red)}$	Vegetation greenness and vigor	2010, 2015, 2020, 2024	Tucker (1979)
MNDWI	$\frac{(Green - SWIR1)}{(Green + SWIR1)}$	Open-water enhancement	2010, 2015, 2020, 2024	Xu (2006)
NDBI	$\frac{(SWIR1 - NIR)}{(SWIR1 + NIR)}$	Built-up characteristics	2010, 2015, 2020, 2024	Zha et al. (2003)
BSI	$\frac{\{(SWIR1 + Red) - (NIR + Blue)\}}{\{(SWIR1 + Red) + (NIR + Blue)\}}$	Bare soil and exposed surfaces	2010, 2015, 2020, 2024	Rikimaru et al. (2002)
EVI	$\frac{2.5(NIR - Red)}{(NIR + 6Red - 7.5Blue + 1)}$	Vegetation vigor with reduced background sensitivity	2010, 2015, 2020, 2024	Huete et al. (2002)
NDRE	$\frac{(B8A - B5)}{(B8A + B5)}$	Canopy chlorophyll / red-edge vegetation response	2020, 2024	Delegido et al. (2011)
Sentinel-2 red-edge bands	B5, B6, B7, B8A	Red-edge spectral response	2020, 2024	Sentinel-2 SR
Sentinel-1 VV	VV backscatter (dB)	Surface structure and dielectric response	2015, 2020, 2024	Sentinel-1 GRD

Sentinel-1 VH	VH backscatter (dB)	Volume scattering and surface structure	2015, 2020, 2024	Sentinel-1 GRD
VH/VV log-ratio	$\boldsymbol{VH_{dB} - VV_{dB}}$	Polarization contrast / structural discrimination	2015, 2020, 2024	Torres et al. (2012)
Elevation	SRTM DEM elevation	Regional physiographic position	2010, 2015, 2020, 2024	SRTM
Slope	Terrain derivative of SRTM DEM	Terrain inclination	2010, 2015, 2020, 2024	SRTM-derived
Aspect	Terrain derivative of SRTM DEM	Terrain orientation	2010, 2015, 2020, 2024	SRTM-derived
TPI	$\boldsymbol{z_i - \bar{z}_{300m}}$	Relative topographic position	2010, 2015, 2020, 2024	SRTM-derived

Training Samples and Validation Strategy

The reference dataset comprised 600 manually delineated polygons interpreted from high-resolution reference imagery, with an initial target of 100 polygons for each of the six LULC classes. The polygons were originally delineated using reference conditions from the 2020–2024 period and were subsequently used to support classification of the earlier epochs. Because transferring contemporary reference labels to earlier dates can introduce temporal-label error where land cover has changed, a temporal-stability screening procedure was applied before model training and validation. Temporal stability was evaluated from the variability of growing-season NDVI over 2015–2024. Annual NDVI representations were generated for each year in this interval, and the interannual standard deviation of NDVI was summarized for each reference polygon. Polygons with an NDVI standard deviation ≥0.15 were excluded from the reusable reference set. The threshold was deliberately permissive so that agricultural polygons exhibiting genuine interannual or seasonal vegetation variability were not systematically eliminated while polygons showing stronger temporal instability were screened out. After this procedure, 572 of the original 600 polygons (95.3%) were retained for classification and validation. Because the stability period begins in 2015, this screening does not independently verify persistence of the assigned class between 2010 and 2015. The 2010 classification therefore relies more strongly on transferred reference labels than the later epochs, and its accuracy estimates are interpreted accordingly. The 572 retained polygons were divided into mutually exclusive training and validation subsets using a deterministic class-stratified procedure. Within each LULC class, a reproducible hash based on polygon-centroid coordinates was used to assign approximately 30% of the polygons to the held-out validation subset and the remainder to model training. This approach ensured representation of all six classes in both subsets and made the split reproducible. The final partition contained 409 training polygons (71.5%) and 163 validation polygons (28.5%). The validation subset was not used to fit the Random Forest classifiers. However, the centroid-hash partition was not designed as a spatial-block cross-validation scheme and does not guarantee geographic independence between neighboring training and validation polygons. Consequently, the reported classification accuracies quantify performance against a reproducible held-out subset of the available reference dataset rather than against an independently collected spatial validation campaign. This distinction was retained when interpreting the accuracy statistics and the subsequent LULC–deformation analyses.

Random Forest Classification and Accuracy Assessment

Random Forest classification was implemented separately for the 2010, 2015, 2020, and 2024 epochs using the algorithm of Breiman (2001). Each epoch-specific classifier contained 500 trees, used a bagging fraction of 0.5, required a minimum leaf population of two samples, and used a fixed random seed of 42. The number of candidate predictors considered at each split followed the default square-root rule for the corresponding epoch-specific feature count. Because the available predictor sets differed among epochs, the four classifiers were trained independently and no fitted model was transferred from one year to another. Classification accuracy was evaluated against the held-out validation subset described above. For each epoch, the validation polygons were classified using the corresponding Random Forest model, and a six-class confusion matrix was constructed from the reference and predicted labels. Overall accuracy (OA) and Cohen's kappa coefficient were calculated from each confusion matrix and are reported in Table 3.

Table 3: Held-out classification accuracy and predictor-set composition for the four LULC epochs.

Epoch	Overall accuracy (%)	Kappa coefficient	Number of predictors	Predictor groups
2010	95.2	0.93	15	Optical bands + spectral indices + topography
2015	96.5	0.95	18	Optical bands + spectral indices + Sentinel-1 GRD + topography
2020	95.5	0.93	23	Optical bands + spectral indices + Sentinel-1 GRD + Sentinel-2 red-edge + topography
2024	95.9	0.94	23	Optical bands + spectral indices + Sentinel-1 GRD + Sentinel-2 red-edge + topography

LULC change and transition matrices

LULC dynamics were quantified by pairwise comparison of the four classified maps over three consecutive intervals: 2010–2015, 2015–2020, and 2020–2024. All calculations were restricted to the common six-county analysis domain and performed on the native 30 m classified grid in EPSG: 32639. For each epoch, class area was calculated from pixels assigned valid class codes 1–6, with each 30 × 30 m pixel contributing 0.0009 km². Net change for each LULC class was calculated as the difference between its mapped area at the end and beginning of the relevant interval; full-period net change was calculated between 2010 and 2024. Pairwise change analysis was restricted to pixels with valid LULC classifications in both epochs of the corresponding interval. A binary change mask distinguished unchanged pixels, for which the class label was identical at both epochs, from changed pixels, for which the class label differed. Changed and unchanged areas and their percentages were calculated relative to the common valid area of each epoch pair so that small differences in classified raster support did not alter the denominator implicitly. Directional transitions were represented using the integer code $T=10C_{t1}+C_{t2}$, where C_{t1} and C_{t2} are the source- and destination-class codes, respectively. Thus, each of the 36 possible source–destination combinations, including class persistence along the matrix diagonal, was uniquely identifiable. Transition areas were obtained from the frequency of each valid transition code multiplied by the 30 m pixel area. Off-diagonal entries were interpreted as gross class-to-class transitions, whereas diagonal entries represented persistence. Because reciprocal transitions can arise from genuine land-cover dynamics as well as classification uncertainty, mixed pixels, seasonal differences, or spectral ambiguity among similar classes, gross transition flows were interpreted together with the corresponding net class-area changes rather than as unambiguous evidence of physical conversion.

Spatiotemporal Subsidence–LULC Linkage

Direct LULC–deformation linkage was evaluated only for epochs with exact calendar-year correspondence between the classified LULC map and the annual SBAS-InSAR LOS-rate field: 2015, 2020, and 2024. Accordingly, the 2015, 2020, and 2024 LULC maps were paired with the annual LOS deformation fields for 2015, 2020, and 2024, respectively. The 2010 LULC map was retained exclusively as the baseline for land-cover change analysis because it predates the Sentinel-1 deformation record. The 2015–2024 mean LOS field was not used for these direct epoch-specific comparisons and was reserved for long-term severity mapping, static well-inventory assessment, and centroid analysis. All direct LULC–deformation comparisons were restricted to the six-county quantitative analysis domain. For each matched epoch, deformation distributions were evaluated for urban, agricultural, bare-land, rangeland, and vegetation classes using the statistical sample described below. Class-level summaries included the number of finite observations, mean, standard deviation, median, and interquartile statistics. Open water was excluded from direct class-level deformation inference because persistent water surfaces provide unreliable interferometric coherence. The resulting design therefore compares land-cover class and deformation within the same calendar year while keeping long-term deformation summaries analytically separate from same-year LULC associations.

Statistical Analysis

The statistical source dataset consisted of 12,766 spatial records obtained by simple-random sampling of the 30 m analysis grid across the six-county domain. Each sampled record carried spatial coordinates together with available annual LOS deformation, epoch-specific LULC, and topographic attributes. A deterministic random subset of 10,000 source points generated with seed 42 was used for the primary class-level statistical analyses, while the complete source pool was evaluated as a sensitivity check. Year-specific analyses used the finite observations available for the corresponding matched epoch; consequently, the effective number of observations could be slightly smaller than the nominal source-sample size where an annual value was unavailable. Nonparametric methods were emphasized because the deformation distributions were strongly skewed and spatially dependent. Point-level significance was therefore interpreted together with effect sizes and dependence-aware sensitivity analyses rather than as evidence from spatially independent observations.

Spatial Autocorrelation Diagnosis

Spatial dependence in the deformation fields was characterized using empirical variograms calculated from coordinates projected to EPSG: 32639. Spherical variogram models were fitted separately to the annual LOS-rate fields for 2015, 2020, and 2024 and to the 2015–2024 mean field. Both the raw fields and fields remaining after removal of a planar spatial trend were examined to assess whether the estimated dependence scale was dominated by a broad regional gradient. The raw model ranges were 13.20 km for 2015, 13.66 km for 2020, 12.41 km for 2024, and 13.40 km for the long-term mean field; the corresponding planar-detrended ranges were 12.92, 13.41, 11.93, and 13.04 km. The median raw annual range was 13.20 km, and this value was rounded upward to define a conservative 14 km spatial scale for the block-level robustness analysis.

Difference Tests and Effect Sizes

For each exactly matched LULC–deformation epoch, overall differences in annual LOS deformation among the five analyzed LULC classes were evaluated using the Kruskal–Wallis test. Epsilon-squared (ε^2) was reported as the principal omnibus effect-size measure, and class-stratified bootstrap resampling with 2,000 replicates was used to derive 95% confidence intervals for ε^2. Pairwise differences among all five classes were evaluated using Mann–Whitney U tests with Holm adjustment for multiple comparisons; these adjusted pairwise results were used to construct the compact-letter groupings shown in Fig. 5. For focused assessment of the agricultural class, agriculture was additionally contrasted with each of the other four classes using signed rank-biserial correlation as an effect-size measure. Because the nominal point count substantially exceeds the number of effectively independent spatial units, the point-level pairwise tests and compact-letter groupings were treated as descriptive inferential summaries rather than as the strongest evidence of spatially independent class separation. For the graphical summaries in Fig. 5, class medians were accompanied by bootstrap 95% intervals. No winsorization, transformation, outlier removal, or display-only subsampling was applied to the plotted deformation distributions. Spearman rank correlations between annual LOS deformation and elevation and slope were also calculated separately for each matched epoch as descriptive checks for topographic covariation.

Robustness Tests

Two complementary analyses were used to evaluate whether the observed class-level patterns were sensitive to spatial dependence. First, distance-based thinning was performed independently for each matched epoch using minimum interpoint spacings of 1, 2, and 3 km and five random seeds at each spacing. LULC class rankings and Kruskal–Wallis ε^2 were calculated for every thinned configuration, allowing the persistence of the principal class-ordering pattern to be assessed across progressively reduced spatial densities. Second, a block-level sign-randomization analysis was conducted using the 14 km dependence scale derived from the variogram analysis. For each matched year and each agriculture-versus-comparison-class contrast, only spatial blocks containing observations from both classes were eligible. Within each eligible block, the median annual LOS deformation rate was calculated separately for agriculture and the comparison class, and the block contrast was defined as the agricultural median minus the comparison-class median. The mean of the eligible block contrasts constituted the observed block-level statistic. Under the null hypothesis of no systematic directional contrast, the signs of the block-level contrasts were randomized while their magnitudes were retained, and a two-sided randomization probability was obtained from the resulting null distribution. Thus, the spatial block rather than the individual sampled point served as the inferential unit. Block-level inference was treated as a conservative robustness assessment because the number of eligible blocks was necessarily much smaller than the nominal point count.

Spatial Well-Inventory Assessment

The static pumping-well inventory was used to evaluate long-term spatial correspondence between recorded well-discharge capacity and the 2015–2024 mean LOS deformation field. This analysis was cross-sectional and was kept analytically separate from the temporally resolved pumping analysis described below. Long-term mean LOS deformation was sampled at the coordinates of wells with the attributes required for the corresponding aggregation. Two complementary aggregations were used. The by-use analysis comprised 3,405 wells in the six-county dataset with recorded use categories and summarized well count, summed recorded operational discharge, and mean long-term LOS deformation for agricultural, industrial–service, and domestic–sanitary uses. The by-plain analysis comprised 3,087 wells assigned to the Tehran–Karaj, Hashtgerd, and Eshtehard plains and summarized the same quantities separately for the three alluvial plains. These populations were intentionally not assumed to be identical because the aggregation criteria differed. Recorded operational discharge was interpreted as reported pumping capacity or an operational-discharge proxy rather than realized annual groundwater abstraction. Consequently, the static well analysis was used as evidence of regional spatial co-location and was not interpreted as a temporal or causal test of aquifer response.

Temporal Pumping–Deformation Lag-Sensitivity Analysis

A separate temporally resolved analysis was used to examine whether annual deformation was associated with contemporaneous or preceding monitored pumping intensity. The analysis was restricted to deep and semi-deep monitoring wells in the Tehran–Karaj, Hashtgerd, and Eshtehard plains. Monthly pumping volume was derived from recorded discharge, daily operating duration, and operating days; where multiple observations occurred for the same site and month, their median was used. The annual site-level pumping predictor was defined as the median of the valid monthly pumping volumes observed within that year and was interpreted as a monitoring-based pumping-intensity index rather than total annual aquifer abstraction. Missing measurements and records indicating non-measurement, shutdown, or dry conditions were not assigned zero pumping in the primary analysis. The primary panel required at least three valid monitored months in every calendar year from 2015 through 2023. This criterion yielded a balanced panel of 23 monitoring sites, comprising 9 sites in Tehran–Karaj, 10 in Hashtgerd, and 4 in Eshtehard. The year 2024 was excluded from the primary pumping analysis because monitoring coverage ended in March 2024 and therefore did not represent a complete calendar year. Annual LOS deformation was sampled from the annual SBAS-InSAR fields at each monitoring-site coordinate. Because the pumping-intensity index was strongly right-skewed, it was log-transformed and standardized before regression. Contemporaneous and lagged associations were evaluated at lags of 0, 1, and 2 years, with annual LOS deformation in year t related to the pumping-intensity index in year $t - k$, where k denotes the lag. The primary specification included site fixed effects and year fixed effects, so the pumping coefficient represented within-site temporal covariation after controlling for time-invariant site characteristics and annual effects common to all monitoring locations. Standard errors were clustered by monitoring site. Two-way-fixed-effects residual Spearman correlations and first-difference models were used as supplementary checks against associations driven primarily by persistent between-site differences or common temporal trends. Sensitivity analyses examined alternative monitoring-coverage requirements, including at least 1, 3, or 6 valid months per year, direct-pixel versus local 3×3 raster sampling, and alternative treatment of selected monitoring-status records. The lag analyses were interpreted as tests of contemporaneous and lagged pumping–deformation association. They were not interpreted as direct estimates of hydraulic-head response time, aquifer-compaction delay, or causal effects of groundwater abstraction.

Centroid and Spatial-Mismatch Analysis

Spatial correspondence between recorded pumping capacity and long-term subsidence intensity was quantified using weighted centroids in EPSG: 32639. The primary recorded-discharge centroid was calculated from 3,061 wells assigned to the Tehran–Karaj, Hashtgerd, and Eshtehard plains that had valid coordinates and positive recorded operational discharge. Well coordinates were weighted by their recorded discharge values. For cartographic comparison, discharge-weighted centroids were also calculated separately for each of the three plains; these plain-specific centroids were used for spatial visualization rather than for separate intraplain distance inference. The subsidence-intensity centroid was calculated from finite pixels of the 2015–2024 mean LOS deformation field within the exact six-county analysis mask that satisfied the operational subsidence criterion. Pixel coordinates were weighted by the absolute magnitude of their negative LOS deformation rates. The primary analysis used a threshold of −20 mm yr^{-1}, and the Euclidean distance between the global three-plain recorded-discharge centroid and the subsidence-intensity centroid was used as a descriptive measure of regional spatial mismatch. Threshold sensitivity was evaluated at −10, −15, −20, −25, and −30 mm yr^{-1}. At each threshold, active-subsidence area, the subsidence-intensity centroid, centroid displacement relative to the primary threshold, and distance from the global recorded-discharge centroid were calculated using identical spatial-domain and weighting rules. Sensitivity was summarized in absolute units and as percentage change relative to the −20 mm yr^{-1} reference. Resampling variability in the global centroid separation was quantified using a two-sample case-resampling bootstrap with 10,000 iterations. In each iteration, the positive-discharge well set and the active-subsidence pixel set were independently resampled with replacement while retaining the coordinates and weight associated with each sampled observation. Recorded-discharge and subsidence-intensity centroids were then calculated from the two resampled sets, and their Euclidean separation was recorded. The bootstrap 95% interval was defined by the 2.5th and 97.5th percentiles of the resulting separation distribution. Threshold sensitivity and case resampling address different aspects of robustness: the former evaluates dependence on the operational definition of active subsidence, whereas the latter evaluates resampling variability of the centroid-separation statistic under the observed spatial support. Because neighboring deformation pixels are spatially dependent, the case-resampling interval was not interpreted as a confidence interval based on spatially independent geodetic observations.

Results and Discussion

Classification Accuracy

Accuracy assessment against the held-out validation subset indicated consistently high classification performance across the four LULC epochs (Table 3). Overall accuracy ranged from 95.2% to 96.5%, while Cohen's kappa coefficients ranged from 0.93 to 0.95 (Cohen, 1960). The 2015 classification showed the highest overall accuracy (96.5%; $\kappa = 0.95$), followed by 2024 (95.9%; $\kappa = 0.94$), 2020 (95.5%; $\kappa = 0.93$), and 2010 (95.2%; $\kappa = 0.93$). These results indicate close agreement between the mapped classes and the held-out reference labels. The accuracy values should nevertheless be interpreted within the validation design described in the Methods.

Although the training and validation subsets were mutually exclusive and generated reproducibly, the centroid-hash partition did not guarantee geographic independence between neighboring reference polygons. The reported accuracies therefore characterize performance against the held-out portion of the available reference dataset rather than against an independently collected spatial validation campaign. Differences in overall accuracy among epochs were modest and should not be attributed to individual sensor or predictor groups because no formal ablation experiment was conducted.

LULC Dynamics and Their Interpretation

LULC trajectories across the common six-county analysis domain were dominated by contraction of agricultural land and net expansion of urban and bare-land surfaces between 2010 and 2024 (Table 4; Fig. 3). Agricultural area declined from 669.08 to 570.09 km², a net loss of 98.99 km² (14.80%), with reductions occurring in all three intervals. Urban land increased by 30.03 km² (10.63%) overall, with most of the net expansion occurring during 2020–2024. Bare land showed a net increase of 66.14 km² despite declining after its 2020 maximum, whereas rangeland changed comparatively little and vegetation increased modestly. Open-water area remained negligible throughout the period. These trajectories indicate substantial restructuring of the cultivated and developed land surface, but with interval-specific differences in both magnitude and direction.

Table 4: Areas and net changes of LULC classes within the common six-county analysis domain, 2010–2024.

Class	2010 (km²)	2015 (km²)	2020 (km²)	2024 (km²)	Net change 2010–2024 (km²)	Relative change (%)
Urban	282.56	275.04	279.50	312.60	+30.03	+10.63
Agriculture	669.08	633.17	582.13	570.09	−98.99	−14.80
Bare land	1,562.97	1,607.45	1,681.26	1,629.10	+66.14	+4.23
Rangeland	1,469.81	1,459.13	1,433.94	1,448.89	−20.92	−1.42
Vegetation	88.04	97.86	95.48	111.65	+23.61	+26.82
Water	3.60	3.44	3.76	3.75	+0.15	+4.10

Note: Areas were calculated from valid class pixels within the identical six-county raster mask at each epoch. The total valid classified area was 4,076.07 km² in 2010 and approximately 4,076.08 km² in 2015, 2020, and 2024.

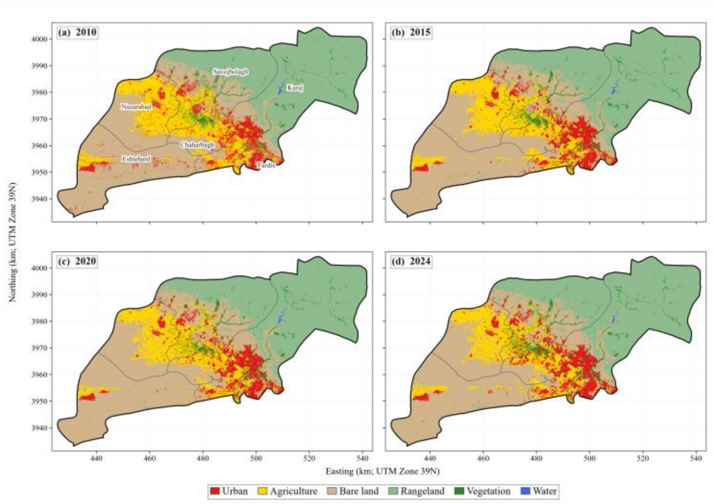

Fig. 3: LULC classification maps for the common six-county analysis domain in 2010, 2015, 2020, and 2024. The maps distinguish urban, agriculture, bare land, rangeland, vegetation, and water classes on the common 30 m analytical grid. The sequence shows a long-term contraction of mapped agricultural land together with net expansion of urban and bare-land surfaces, although the magnitude and direction of change vary among intervals. Taleghan lies outside the quantitative analysis domain.

The transition matrices clarify the pathways underlying these net changes, although their interpretation requires caution. The transition analysis showed that most of the six-county domain retained the same assigned LULC class between consecutive epochs. Unchanged pixels accounted for 89.28% of the common valid area during 2010–2015, 90.78% during 2015–2020, and 91.06% during 2020–2024. Correspondingly, the area assigned to a different class declined from 436.90 km² (10.72%) in the first interval to 375.66 km² (9.22%) in the second and 364.39 km² (8.94%) in the final interval. The gross transition matrices nevertheless contained bidirectional exchanges among spectrally similar classes, particularly agriculture, bare land, and transitional vegetation surfaces. Because some reverse transitions may reflect seasonal spectral variability, mixed pixels, fallow conditions, or classification uncertainty rather than permanent land-use conversion, net class-area trajectories provide the more conservative basis for interpreting long-term structural LULC change. Overall, the cultivated footprint contracted while urban and bare-land surfaces expanded. Importantly, the strong post-2020 urban increase does not parallel the deformation ranking reported below, in which agricultural land consistently occupies the more-negative part of the annual LOS distribution. LULC classes are therefore interpreted as spatial indicators of land-surface use and associated groundwater-demand regimes rather than direct causal controls on deformation. The same-year LULC–deformation analysis below tests this spatial association explicitly.

Spatial pattern and severity zonation of land subsidence

The 2015–2024 mean LOS deformation field showed pronounced spatial heterogeneity across the six-county analysis domain. The rasterized six-county mask covered 4,079.15 km², of which 3,306.31 km² contained finite long-term InSAR observations; the remaining 772.84 km² lacked valid long-term deformation support and were excluded from deformation-rate and severity-area statistics. Within the valid InSAR support, the mean LOS deformation rate was −23.24 mm yr⁻¹, whereas the median was only −2.80 mm yr⁻¹, indicating a strongly left-skewed distribution dominated by localized zones of rapid negative deformation. Pixel-level mean LOS rates ranged from −408.05 to +162.61 mm yr⁻¹. Positive LOS values were retained in the statistical distribution but were not interpreted as direct vertical uplift because the deformation field was derived from a single descending viewing geometry. Using the operational subsidence threshold of −20 mm yr⁻¹, 636.14 km², corresponding to 19.24% of the valid InSAR support, was classified as actively subsiding, whereas 2,670.17 km² (80.76%) fell within the stable/low-deformation class. The active area comprised 127.26 km² of slight subsidence (3.85% of valid support), 243.26 km² of moderate subsidence (7.36%), 206.00 km² of severe subsidence (6.23%), and 59.63 km² of critical subsidence (1.80%). Severe and critical subsidence together occupied 265.62 km², or 8.03% of the valid deformation footprint. Thus, the most intense deformation was spatially concentrated rather than uniformly distributed across the study domain. Deformation within the active-subsidence zone was substantial. Pixels with mean rates ≤ −20 mm yr⁻¹ had a mean rate of −112.54 mm yr⁻¹ and a median of −103.41 mm yr⁻¹. The 5th percentile of the active distribution was −251.74 mm yr⁻¹, indicating that approximately 5% of active pixels exhibited LOS rates more negative than about −252 mm yr⁻¹. The strong contrast between the domain-wide median and the active-zone distribution demonstrates that the regional mean is governed disproportionately by spatially confined subsidence bowls. Spatial clustering was also evident in the geostatistical structure of the deformation field. The empirical variogram of the 2015–2024 mean LOS rate yielded a spherical-model range of 13.40 km, while the annual fields used in the LULC linkage analysis had raw variogram ranges of 13.20 km in 2015, 13.66 km in 2020, and 12.41 km in 2024. Comparable ranges after planar detrending indicate that this spatial dependence was not solely attributable to a broad regional trend. The most pronounced subsidence was concentrated in the western and central alluvial sectors, particularly within the Hashtgerd system, whereas deformation was generally less intense across the Eshtehard Plain. The ten-year mean field therefore represents the long-term spatial organization of deformation, while year-specific LOS layers were used separately to evaluate temporal correspondence with LULC.

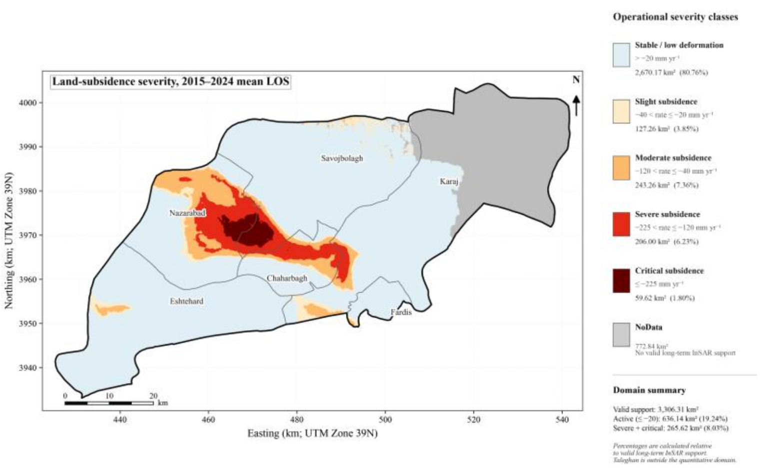

Fig. 4: Land-subsidence severity zonation within the six-county analysis domain based on the 2015–2024 mean LOS deformation rate. Five operational classes are shown: stable/low deformation (> −20 mm yr⁻¹), slight (−40 < rate ≤ −20 mm yr⁻¹), moderate (−120 < rate ≤ −40 mm yr⁻¹), severe (−225 < rate ≤ −120 mm yr⁻¹), and critical (≤ −225 mm yr⁻¹). Areas without valid long-term InSAR support are retained as NoData and excluded from severity-area percentages. Taleghan lies outside the quantitative analysis domain.

The regional pattern is broadly consistent with previous studies documenting substantial subsidence in the Hashtgerd and Tehran–Karaj aquifer systems. In Hashtgerd, SBAS time-series analysis reported cumulative subsidence of 18–320 mm during 2017–2022 and a significant relationship with groundwater-level decline (Rostami et al, 2023), while Sentinel-1 observations for 2014–2023 documented cumulative deformation exceeding 90 cm and local rates greater than 180 mm yr⁻¹ (Kalantarian et al, 2025).

In Tehran–Karaj, rates approaching 158 mm yr⁻¹ and an approximately two-year delay between groundwater-level decline and peak surface response have been reported (Shiri et al, 2024). Previous work has also indicated comparatively weaker and more localized deformation in Eshtehard (Norouzi et al, 2025). Because these studies differ in temporal window, interferometric processing, deformation metric, spatial support, and LOS geometry, they provide regional context rather than pixel-level validation of the present deformation field.

Same-Year LULC–Deformation Associations

Exact same-year comparison of the LULC and annual LOS deformation datasets revealed a persistent association between agricultural land and the most negative deformation rates at all three analyzed epochs (Table 5). In the primary 10,000-point sample, agricultural land had mean LOS rates of −71.01 mm yr^{-1} in 2015, −98.12 mm yr^{-1} in 2020, and −93.73 mm yr^{-1} in 2024. The corresponding medians were −50.93, −79.67, and −65.56 mm yr^{-1}, respectively. Agriculture therefore occupied the most negative position in both mean and median deformation among the five analyzed LULC classes in each matched year. The ordering of the remaining LULC classes varied among epochs (Table 5). Urban and vegetation classes generally showed intermediate negative rates, bare land remained comparatively weakly deformed in all three years, and rangeland shifted toward more-negative values by 2024. The temporally persistent feature was therefore not a common trend across all classes but the repeated position of agricultural land at the most-negative end of both the mean and median deformation distributions.

Table 5: Same-year LOS deformation statistics for the five analyzed LULC classes in 2015, 2020, and 2024.

LULC class	2015 mean	2015 median	2020 mean	2020 median	2024 mean	2024 median
Agriculture	−71.01	−50.93	−98.12	−79.67	−93.73	−65.56
Vegetation	−35.27	−3.56	−27.92	−6.22	−49.29	−7.45
Urban	−24.87	−4.49	−43.48	−7.99	−43.33	−0.10
Rangeland	+1.47	+1.43	−4.76	−3.23	−22.07	−20.64
Bare land	−4.58	−2.20	−9.51	−2.87	−6.24	−0.30

Note: Each LULC map was paired with the annual LOS deformation layer from the same calendar year. Statistics are based on the deterministic 10,000-point primary analysis sample (seed = 42); open-water pixels were excluded because of unreliable interferometric coherence. Negative values indicate motion away from the satellite along the descending LOS and are interpreted here as the subsidence-dominated component of the deformation field. The primary sample contained 10,000 finite observations in 2015 and 2020 and 9,999 finite observations in 2024.

The same-year deformation distributions differed substantially among LULC classes at all three epochs. In the primary 10,000-point sample, Kruskal–Wallis effect sizes were ε^2 = 0.378 for 2015, 0.222 for 2020, and 0.273 for 2024. The corresponding results from the complete 12,766-point source pool were very similar (ε^2 = 0.371, 0.216, and 0.271, respectively), indicating that the estimated magnitude of the class association was not sensitive to the primary sampling step. Nominal Kruskal–Wallis p-values were <0.001 in all three years; however, because individual observations were spatially autocorrelated, inference emphasized effect magnitude and spatial robustness rather than pixel-level significance alone. Point-level pairwise comparisons consistently placed agriculture toward more-negative deformation than the other LULC classes. The agriculture–bare-land contrast was especially pronounced, with signed rank-biserial correlations of −0.773 in 2015, −0.680 in 2020, and −0.647 in 2024; the negative sign denotes more-negative LOS deformation over agricultural land. All agriculture-versus-other-class comparisons remained significant after Holm adjustment in the primary point sample, but these tests were treated as descriptive because the nominal sample size exceeds the effective number of spatially independent observations. Spatial thinning supported the stability of the principal class ranking. Across the fifteen distance–seed configurations evaluated for each year, agriculture retained the most-negative class mean in 14 of 15 configurations in 2015, all 15 configurations in 2020, and 13 of 15 configurations in 2024, corresponding to 42 of 45 configurations overall. Median ε^2 values remained substantial across thinning distances: approximately 0.367–0.393 in 2015, 0.227–0.261 in 2020, and 0.263–0.287 in 2024. The more conservative block-level analysis produced a narrower pattern of support. The agriculture–bare-land contrast remained significant at the 14 km block scale in every matched year (p = 0.0001 in 2015, p = 0.0005 in 2020, and p = 0.0017 in 2024). Other contrasts were less consistent: agriculture differed from urban land at the block level in none of the three years, while agriculture–rangeland and agriculture–vegetation contrasts were supported only in selected epochs. The most reproducible spatially robust result was therefore the persistent separation between agricultural and bare-land deformation distributions rather than universal separation of agriculture from every other class.

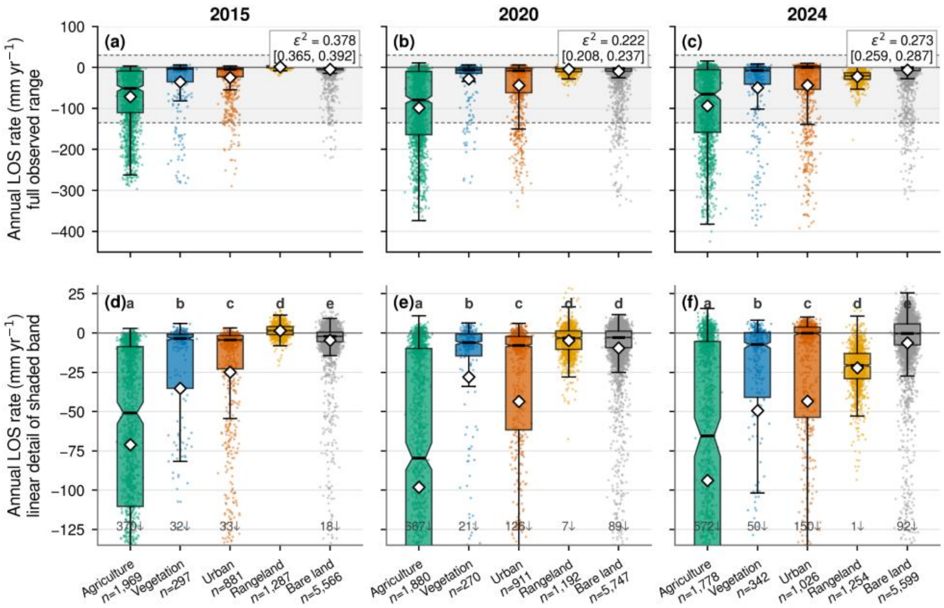

Fig. 5: Same-year distributions of annual LOS deformation rates among five LULC classes in (a, d) 2015, (b, e) 2020, and (c, f) 2024. Each column pairs the LULC classification with the annual LOS deformation field from the same calendar year. Panels (a)–(c) show the complete observed distributions on a common linear vertical scale, whereas panels (d)–(f) present linear enlargements of the shaded ranges in the corresponding upper panels. The numbers at the base of the lower panels indicate the count of observations falling below the displayed magnified range. No winsorization, transformation, outlier removal, or display-only subsampling was applied; box plots, means, and plotted points all derive from the same deterministic 10,000-point primary analysis sample (seed = 42). Boxes represent the interquartile range, notches indicate bootstrap 95% intervals for the class medians, central black lines denote medians, white diamonds denote class means, and whiskers extend to 1.5 × the interquartile range. Insets report Kruskal–Wallis ε^2 effect sizes with stratified bootstrap 95% intervals (2,000 replicates). Lower-case letters summarize point-level pairwise comparisons based on Mann–Whitney U tests with Holm adjustment (α = 0.05); classes sharing a letter were not distinguishable in those comparisons. These pairwise contrasts are descriptive because the nominal sample size exceeds the effective number of spatially independent observations; spatial robustness was evaluated separately using distance thinning and 14-km block-level analysis. Colours follow a colour-blind-safe palette and are redundant with the categorical axis labels. Open-water pixels were excluded because persistent water surfaces provide unreliable interferometric coherence. Negative LOS values indicate motion away from the satellite along the descending line of sight and are interpreted here as the subsidence-dominated component of the deformation field. Agricultural land occupies the most negative position in both mean and median deformation in all three matched years, whereas the relative ordering of the remaining classes varies among epochs.

Topographic covariation was not temporally consistent across the three matched epochs. In the primary sample, Spearman correlations between LOS deformation and elevation were +0.179 in 2015, +0.136 in 2020, and −0.267 in 2024, while correlations with slope were +0.349, +0.240, and −0.066, respectively. The change in both magnitude and sign through time indicates that a simple monotonic relationship with elevation or slope cannot account for the persistent position of agricultural land within the deformation distributions. These bivariate tests do not exclude confounding by sedimentology, aquifer geometry, groundwater conditions, or spatially structured land use, but they show that the observed agricultural association is not reducible to a stable elevation or slope gradient alone. Groundwater use is therefore evaluated independently below using the well inventory and the temporally resolved monitoring dataset.

Groundwater Pumping and Subsidence

Static Well-Inventory Patterns

The static pumping-well inventory provided a complementary spatial assessment of the relationship between recorded groundwater use and long-term deformation. The use-based analysis comprised 3,405 wells with valid long-term deformation values and recorded groundwater-use categories. Agricultural wells accounted for 1,606 records and a combined recorded operational discharge of 12,486.68 L s^{-1}; their locations had a mean 2015–2024 LOS deformation rate of −80.93 mm yr^{-1}. Industrial–service wells comprised 1,452 records with 4,149.18 L s^{-1} of recorded discharge and a mean LOS rate of −38.68 mm yr^{-1}, while 347 domestic–sanitary wells represented 5,371.33 L s^{-1} and a mean rate of −41.23 mm yr^{-1}. Thus, agricultural-well locations occupied substantially more-negative portions of the long-term deformation field than the other recorded use categories. Plain-level aggregation produced a different but complementary pattern (Table 6). The Tehran–Karaj Plain contained 1,923 wells with 10,921.15 L s^{-1} of recorded operational discharge and a mean long-term LOS rate of −35.40 mm yr^{-1}. Hashtgerd contained 1,060 wells with 7,475.69 L s^{-1} of recorded discharge but a substantially more-negative mean LOS rate of −95.37 mm yr^{-1}. Eshtehard contained 104 wells with 789.81 L s^{-1} of recorded discharge and had the least-negative mean rate, −12.64 mm yr^{-1}. Recorded pumping-capacity ranking therefore did not parallel deformation ranking among the three plains: Tehran–Karaj contained the largest recorded capacity, whereas the strongest negative deformation at well locations occurred in Hashtgerd.

The LULC- and well-based analyses are complementary rather than statistically independent because both rely on the same InSAR deformation product. Moreover, the two well aggregations use different analytical populations and recorded operational discharge represents reported pumping capacity rather than realized annual abstraction. The static inventory therefore supports a regional spatial association between agricultural groundwater-use environments and stronger long-term deformation, but it does not by itself establish a temporal pumping response or causal aquifer relationship. Such an interpretation is physically consistent with compaction of fine-grained alluvial deposits under increased effective stress following groundwater-level decline (Terzaghi, 1943; Galloway et al, 1999), but temporal response requires independently resolved pumping or hydraulic-head information.

Table 6: Static pumping-well inventory summarized by alluvial plain and groundwater-use category.

Aggregation	Group	Number of wells	Total recorded operational discharge (L s^{-1})	Mean 2015–2024 LOS deformation rate (mm yr^{-1})
By alluvial plain	Tehran–Karaj	1,923	10,921.15	−35.40
By alluvial plain	Hashtgerd	1,060	7,475.69	−95.37
By alluvial plain	Eshtehard	104	789.81	−12.64
By use type	Agriculture	1,606	12,486.68	−80.93
By use type	Industrial–service	1,452	4,149.18	−38.68
By use type	Domestic–sanitary	347	5,371.33	−41.23

Note: The by-plain summary is restricted to wells assigned to the Tehran–Karaj, Hashtgerd, and Eshtehard alluvial plains, whereas the by-use summary includes all validated well records with an assigned use category and valid long-term deformation value. Recorded operational discharge represents reported pumping capacity rather than measured annual groundwater abstraction; totals from the two aggregation schemes should therefore not be compared directly.

Temporal Pumping–Deformation Lag-Sensitivity

The temporally resolved analysis used a balanced panel of 23 deep and semi-deep monitoring wells with at least three valid pumping observations in every year from 2015 through 2023. The panel comprised nine sites in Tehran–Karaj, ten in Hashtgerd, and four in Eshtehard. The pumping predictor was the standardized log-transformed site-year median of observed monthly pumping volume and therefore represents a monitoring-based pumping-intensity index rather than total annual groundwater abstraction. The primary two-way fixed-effects models provided no evidence of a robust contemporaneous or one-to-two-year lagged association between monitored pumping intensity and annual LOS deformation (Table 7). At lag 0, a one-standard-deviation increase in log-transformed pumping intensity was associated with a coefficient of −3.59 mm yr^{-1} (95% CI: −26.48 to 19.29; p = 0.748). The corresponding coefficient was −9.61 mm yr^{-1} at lag 1 (95% CI: −29.10 to 9.88; p = 0.318) and +2.68 mm yr^{-1} at lag 2 (95% CI: −13.73 to 19.08; p = 0.738). All three confidence intervals included zero. First-difference rank correlations supported the same general interpretation. Associations between year-to-year changes in the pumping-intensity index and changes in annual LOS deformation were weak at lag 0 (ρ = −0.017, p = 0.823), lag 1 (ρ = −0.009, p = 0.900), and lag 2 (ρ = +0.047, p = 0.553). Sensitivity analysis likewise showed that the lag-0 coefficient remained negative across all 12 tested specifications but was nominally significant in none of them. At lag 1, six of 12 coefficients were negative and only two reached nominal $p < 0.05$, whereas four of 12 lag-2 coefficients were negative and none reached nominal significance. The absence of a reproducible coefficient pattern across lag structures and sensitivity specifications does not support a uniquely resolved short-term pumping–deformation lag. These temporal results do not imply that groundwater withdrawal is unrelated to aquifer compaction. The pumping-intensity index is not equivalent to hydraulic-head decline, and deformation may reflect cumulative effective-stress history, delayed aquitard drainage, recharge variability, sediment compressibility, and pumping prior to the monitoring window. The approximately two-year response reported from groundwater-level observations in Tehran–Karaj (Shiri et al, 2024) is therefore useful hydrogeological context but is not directly equivalent to the pumping-intensity lag tested here.

Table 7: Within-site associations between the monitoring-based pumping-intensity index and annual LOS deformation at lags of 0–2 years.

Lag (yr)	Observations	Monitoring sites	β (mm yr⁻¹ per 1 SD higher log pumping)	95% CI	Cluster-robust p
0	207	23	−3.59	−26.48 to 19.29	0.748
1	207	23	−9.61	−29.10 to 9.88	0.318
2	184	23	+2.68	−13.73 to 19.08	0.738

Note: β values are from models including monitoring-site and year fixed effects, with standard errors clustered by monitoring site. Lag 0 relates pumping and deformation within the same year; lags 1 and 2 relate deformation to pumping measured one and two years earlier, respectively. The analysis tests temporal association and does not estimate hydraulic-head response time or establish causality.

Spatial Mismatch between Recorded-Discharge

The static-well results revealed that recorded pumping capacity and deformation severity do not share the same regional spatial distribution, motivating a direct comparison of their weighted spatial centers. This distinction is especially evident between Tehran–Karaj, which contains the largest recorded discharge capacity, and Hashtgerd, where long-term deformation at well locations is substantially more negative. The recorded-discharge-weighted centroid of the 3,061 positive-discharge wells across the three analyzed plains was located at UTM coordinates 483,593.48 m E and 3,965,102.90 m N. Using the −20 mm yr^{-1} operational threshold, the subsidence-intensity-weighted centroid was separated from this global discharge centroid by 15.16 km (Fig. 6a). Case resampling yielded a bootstrap 95% interval of 14.22–16.11 km for the centroid separation (Fig. 6c), indicating that the regional offset remained substantial under resampling of the contributing spatial observations. The resampled separation distribution therefore remained centered near the observed regional offset, although this interval does not account for all sources of spatial dependence, measurement uncertainty, or model uncertainty. Relative to the global discharge centroid, the subsidence centroid lay approximately 14.00 km farther west and 5.83 km farther north, corresponding to a west-northwest direction of approximately 293°. The centroid separation therefore quantifies a regional mismatch between the spatial concentration of recorded pumping capacity and the spatial concentration of long-term subsidence intensity rather than a physical displacement or aquifer-response distance. The centroid-level spatial mismatch showed limited sensitivity to the operational threshold used to delineate active subsidence (Fig. 6b; Table 8). Across thresholds from −30 to −10 mm yr^{-1}, active-subsidence area increased from 561.03 to 819.92 km^2, whereas the distance between the global recorded-discharge and subsidence-intensity centroids changed only from 15.28 to 15.00 km. When expressed relative to the primary −20 mm yr^{-1} reference, the full threshold-dependent span was 40.7% for active-subsidence area but only 1.9% for centroid separation; the mapped area was therefore approximately 21 times more threshold-sensitive than the centroid-distance metric. Moreover, the subsidence centroid itself remained within 0.22 km of its −20 mm yr^{-1} position throughout the tested threshold range. Thus, although the mapped extent of active subsidence depends appreciably on the selected operational criterion, the principal centroid-level spatial mismatch is comparatively insensitive to the exact threshold.

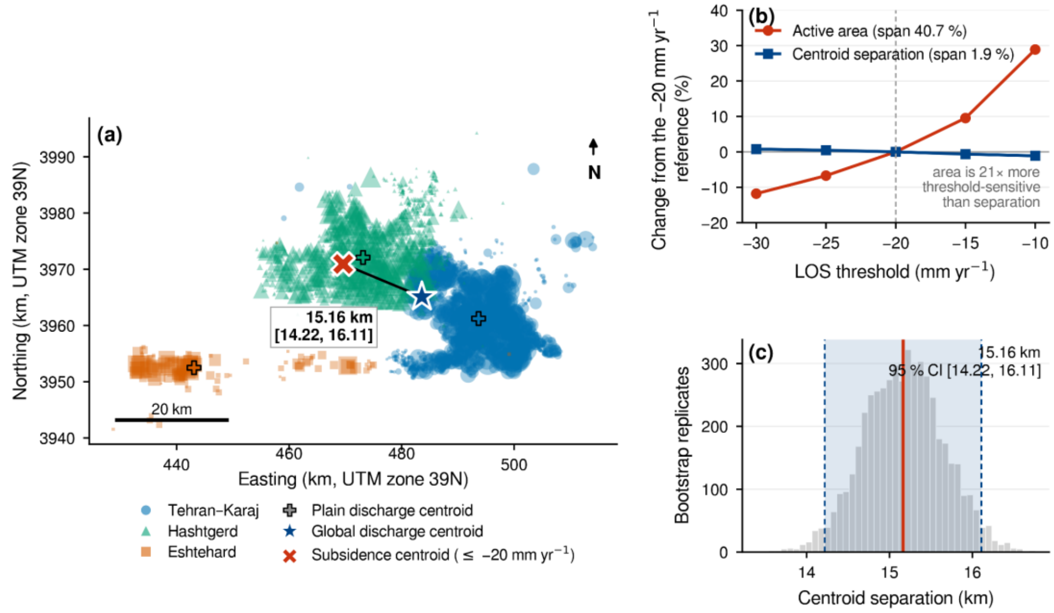

Fig. 6: Spatial mismatch between recorded pumping capacity and long-term subsidence intensity, together with threshold and resampling sensitivity of the centroid separation. (a) Spatial distribution of pumping wells assigned to the Tehran–Karaj, Hashtgerd, and Eshtehard plains and their discharge-weighted centroids. Circles, triangles, and squares distinguish wells assigned to Tehran–Karaj, Hashtgerd, and Eshtehard, respectively. Crosses indicate the discharge-weighted centroid calculated separately for each plain, the blue star marks the global three-plain recorded-discharge centroid, and the red cross marks the subsidence-intensity centroid derived from pixels with 2015–2024 mean LOS rates ≤ −20 mm yr^{-1} and weighted by the absolute magnitude of negative deformation. The global discharge centroid is based on 3,061 wells with valid coordinates and positive recorded operational discharge. At the primary −20 mm yr^{-1} threshold, the global discharge and subsidence centroids are separated by 15.16 km; the bootstrap 95% interval is 14.22–16.11 km. (b) Sensitivity of mapped active-subsidence area and centroid separation to LOS-rate thresholds from −30 to −10 mm yr^{-1}, expressed as percentage change relative to the primary −20 mm yr^{-1} reference. Across the tested range, active-subsidence area spans 40.7% relative to the reference value, whereas centroid separation spans only 1.9%, indicating that mapped area is approximately 21 times more threshold-sensitive than the centroid separation. (c) Bootstrap distribution of the global centroid separation. The solid vertical line marks the observed separation of 15.16 km, and the dashed lines delimit its bootstrap 95% interval of 14.22–16.11 km.

The centroid mismatch indicates that recorded pumping capacity alone does not determine the spatial location of the strongest long-term deformation. This interpretation is consistent with the plain-level contrast between Tehran–Karaj and Hashtgerd: the former contains the larger share of recorded discharge, whereas the latter exhibits substantially more-negative deformation. The threshold-sensitivity analysis further shows that this spatial offset is a persistent feature of the deformation field rather than a consequence of selecting a particular operational subsidence threshold. Hydrogeological heterogeneity provides a physically plausible framework for this pattern. Surface deformation in an alluvial aquifer depends not only on groundwater withdrawal but also on groundwater-head history, recharge, aquifer and aquitard geometry, the thickness and compressibility of fine-grained sediments, and the degree to which effective-stress changes are accommodated elastically or inelastically. Tehran–Karaj receives substantial surface-water input from the Karaj River, whereas Hashtgerd depends more strongly on the smaller Kordan system and includes multilayered alluvial deposits containing fine-grained interbeds. These differences are consistent with spatially variable susceptibility to compaction, although recharge, pore-pressure evolution, and sediment compressibility were not measured directly in this study.

Table 8: Sensitivity of active-subsidence extent and centroid separation to the operational LOS-rate threshold.

LOS threshold (mm yr^{-1})	Active-subsidence area (km^2)	Centroid separation (km)	Subsidence-centroid shift relative to −20 case (km)
−10	819.92	15.00	0.22
−15	696.82	15.07	0.14
−20	636.14	15.16	0.00

LOS threshold (mm yr⁻¹)	Active-subsidence area (km²)	Centroid separation (km)	Subsidence-centroid shift relative to −20 case (km)
−25	593.40	15.23	0.09
−30	561.03	15.28	0.15

Note: Active-subsidence areas are calculated from finite pixels of the 2015–2024 mean LOS deformation field within the exact six-county analysis mask. Subsidence centroids are weighted by the absolute magnitude of negative LOS rates, and centroid separation is measured relative to the recorded-discharge-weighted centroid of 3,061 wells with valid coordinates and positive recorded operational discharge in the Tehran–Karaj, Hashtgerd, and Eshtehard plains.

The temporal monitoring analysis reinforces the need for this more nuanced interpretation. No reproducible contemporaneous, one-year, or two-year association was detected between within-site variation in monitored pumping intensity and annual LOS deformation after accounting for site and year effects. Spatial coincidence between agricultural groundwater use and stronger subsidence therefore coexists with a short-term temporal relationship that was not reproducibly resolved by the available monitoring data. A complete process-based explanation would require continuous piezometric observations, actual abstraction volumes and pumping durations, detailed lithological information, sediment-compressibility measurements, and coupled groundwater-flow and consolidation modeling.

Methodological Implications of Autocorrelation-Aware Inference

Spatial autocorrelation materially constrained point-level inference. Raw annual variogram ranges were 13.20, 13.66, and 12.41 km in 2015, 2020, and 2024, respectively, with similar estimates after planar detrending; a conservative 14 km block scale was therefore used for robustness analysis. The nominal 10,000-point sample should consequently not be interpreted as 10,000 spatially independent observations. Nevertheless, agriculture retained the most-negative mean deformation in 42 of 45 spatial-thinning configurations, and the agriculture–bare-land contrast remained supported at the 14 km block scale in all three matched years. Other agriculture-versus-class contrasts were less consistent at block scale, making the agriculture–bare-land separation the most reproducible pairwise result. These findings illustrate why dense InSAR samples should be interpreted using effect magnitude and spatial robustness rather than nominal pixel-level significance alone. The compact-letter groupings in Fig. 5 summarize point-level Holm-adjusted comparisons, whereas thinning and block-level analyses provide the stronger assessment of robustness to spatial dependence. Even this robustness does not imply causality: statistical separation among LULC classes demonstrates reproducible spatial association, not that land-use class itself produces the observed deformation.

Limitations and uncertainties

Several limitations constrain the scope of inference. First, deformation was measured from a single descending Sentinel-1 geometry and therefore represents LOS motion rather than independently resolved vertical displacement. Negative LOS rates are interpreted as the subsidence-dominated component, but horizontal and vertical contributions cannot be separated without complementary viewing geometries. No concurrent GNSS or precise-leveling observations were available for independent geodetic validation, and no dedicated atmospheric-phase-screen correction was applied. Although acquisitions affected by unfavorable atmospheric conditions were screened before time-series inversion, residual tropospheric effects cannot be excluded. Long-term InSAR observations were finite over 3,306.31 km² of the 4,079.15 km² rasterized six-county domain, leaving 772.84 km² (18.95%) without valid support; interpretation is therefore strongest for persistent spatial patterns within the observed footprint rather than isolated extreme pixels or areas lacking valid observations. Second, the LULC analysis combines Landsat-based classifications for 2010 and 2015 with Sentinel-2-based classifications for 2020 and 2024. Although the data were harmonized to a common 30 m analytical grid and direct deformation comparisons use exact same-year observations in 2015, 2020, and 2024, sensor and predictor differences can still contribute to apparent interepoch change. The held-out validation design was reproducible but not guaranteed spatially independent, and the temporal-stability screen did not extend to 2010. Classification uncertainty is also uneven among spectrally overlapping surface types; consequently, net class-area trajectories are interpreted more confidently than individual gross transition pathways. Third, the groundwater datasets constrain both spatial and temporal attribution. Recorded operational discharge in the static inventory represents reported pumping capacity rather than realized annual abstraction. The temporal analysis is based on only 23 deep and semi-deep monitoring sites satisfying the balanced-panel criterion for 2015–2023, and incomplete pumping records were retained as missing rather than converted to zero. The resulting site-year variable is therefore a monitoring-based pumping-intensity index, not annual aquifer abstraction. Failure to detect a robust contemporaneous or one-to-two-year association does not demonstrate that groundwater withdrawal is unrelated to compaction or that delayed response is absent; pumping intensity is not equivalent to hydraulic-head decline, and longer, nonlinear, or spatially variable consolidation responses may remain unresolved. Finally, the hydrogeological and centroid interpretations are descriptive rather than process-complete. The contrast between Tehran–Karaj and Hashtgerd is consistent with spatial differences in recharge, aquifer architecture, fine-grained sediment abundance, and compressibility, but these controls were not measured jointly. Likewise, the 15.16 km centroid separation summarizes the spatial offset between two weighted distributions and is neither a hydraulic-response distance nor a physical displacement. Threshold sensitivity and case resampling demonstrate robustness to specific analytical choices, while spatial autocorrelation still reduces the effective information content relative to the nominal observation count. Definitive process attribution would require complementary geodetic observations, continuous piezometry, actual abstraction histories, detailed stratigraphy, sediment-compressibility measurements, and coupled groundwater-flow and consolidation modeling.

Management Implications for Spatially Targeted Subsidence Management

Subsidence management in the Alborz alluvial plains should not rely on recorded pumping capacity alone. Tehran–Karaj contains the largest recorded operational discharge, whereas Hashtgerd exhibits substantially more-negative long-term deformation, and the 15.16 km centroid separation further demonstrates that reported pumping capacity and deformation intensity are spatially offset. Hashtgerd therefore warrants particularly close monitoring, not because the present analysis demonstrates a larger response per unit pumping, but because the controls responsible for its strong deformation remain incompletely resolved. Denser piezometry, measurement of actual abstraction and pumping duration, updated well inventories, and continued InSAR monitoring are needed before site-specific abstraction, recharge, or allocation interventions can be evaluated. The LULC results provide a complementary basis for spatial prioritization. Agricultural land consistently occupied the most-negative part of the annual deformation distributions in 2015, 2020, and 2024, and agricultural wells were located within substantially more-negative portions of the long-term deformation field than the other recorded use categories. At the same time, the temporal monitoring analysis did not identify a reproducible contemporaneous or one-to-two-year relationship between within-site pumping-intensity variation and annual LOS deformation. These findings argue against interpreting agricultural land cover as a direct causal predictor of annual subsidence, but they support using agricultural groundwater-use zones as one component of a broader monitoring framework. Land-use planning should therefore consider persistent deformation jointly with groundwater conditions and exposure, particularly where continuing urban expansion places infrastructure or population over actively deforming ground. The severity map should likewise be used as a deformation-screening product rather than as a complete risk map. Areas of severe or critical deformation can be prioritized for detailed ground investigation and repeated monitoring, but decisions concerning infrastructure, urban expansion, or land development require additional information on exposure, vulnerability, foundation conditions, fissuring, and local geotechnical properties. More broadly, the strongest practical implication of the analysis is the need for an integrated monitoring system linking InSAR deformation, continuous groundwater levels, measured abstraction volumes and pumping durations, updated well information, LULC change, and infrastructure or population exposure. Such integration would allow future management to distinguish locations of high pumping pressure, high deformation susceptibility, and high societal exposure instead of treating them as spatially equivalent.

Conclusion

This study demonstrates that land subsidence across the southern alluvial plains of Alborz Province is characterized by a persistent but spatially non-uniform association with groundwater-dependent land use, and that this association cannot be reduced to recorded pumping capacity alone. Integration of annual Sentinel-1 SBAS-InSAR LOS deformation for 2015–2024 with LULC maps for 2010, 2015, 2020, and 2024 showed that the six-county analysis domain underwent a sustained contraction of mapped agricultural land alongside net expansion of urban and bare-land surfaces. Agricultural area declined by 98.99 km² (14.80%) between 2010 and 2024, while urban area increased by 30.03 km². At the same time, the long-term deformation field was strongly heterogeneous: 636.14 km², or 19.24% of the valid long-term InSAR footprint, satisfied the study's operational active-subsidence criterion of ≤ -20 mm yr^{-1}. These results show that broad land-surface transformation and intense deformation coexist within the same regional system but should not be interpreted as mechanically equivalent processes. Exact same-year comparisons provide the strongest evidence for the LULC–deformation relationship. Agricultural land occupied the most-negative position in both mean and median annual LOS deformation in 2015, 2020, and 2024, with Kruskal–Wallis ε^2 values of 0.378, 0.222, and 0.273, respectively. This class-level pattern remained broadly stable under spatial thinning, with agriculture retaining the most-negative mean deformation in 42 of 45 thinning configurations. However, the 14 km block-level analysis showed that the most consistently supported pairwise contrast was agriculture versus bare land, rather than universal separation of agriculture from every other class. The principal inference is therefore not that agricultural land cover itself causes subsidence, but that agricultural groundwater-use environments repeatedly coincide with the more negative part of the regional deformation field, and that this association persists after explicit consideration of spatial dependence. The groundwater analyses further distinguish spatial correspondence from temporal response. Agricultural wells were located within substantially more-negative portions of the 2015–2024 deformation field than industrial–service or domestic–sanitary wells, yet plain-level pumping capacity and deformation severity did not exhibit the same spatial ranking. Tehran–Karaj contained the largest recorded operational discharge across the three analyzed plains, whereas Hashtgerd exhibited substantially more-negative long-term deformation at well locations. Consistent with this mismatch, the recorded-discharge-weighted centroid of 3,061 positive-discharge wells was separated from the subsidence-intensity centroid by 15.16 km. This separation remained between approximately 15.00 and 15.28 km across operational thresholds from -10 to -30 mm yr^{-1}, whereas the mapped active-subsidence area was much more threshold-sensitive. The centroid result therefore identifies a persistent regional spatial mismatch between reported pumping capacity and subsidence intensity rather than a hydraulic-response distance or physical displacement. In contrast to these persistent spatial relationships, the temporally resolved monitoring dataset did not identify a reproducible contemporaneous, one-year, or two-year association between within-site variation in the monitoring-based pumping-intensity index and annual LOS deformation. The primary fixed-effects coefficients at all three lags had confidence intervals spanning zero, and first-difference and sensitivity analyses did not reveal a stable short-term lag structure. This finding should not be interpreted as evidence that groundwater withdrawal is unrelated to compaction. Rather, it indicates that the available 23-site monitoring panel and pumping-intensity proxy do not resolve a unique short-term deformation response. Pumping intensity is not equivalent to hydraulic-head decline, and aquifer deformation may integrate antecedent groundwater conditions, delayed drainage of fine-grained layers, recharge variability, sediment compressibility, and cumulative effective-stress history. Taken together, the results support a conceptual model in which groundwater use is an important regional component of the subsidence system, while hydrogeological heterogeneity governs where a given groundwater-stress regime is translated into stronger surface deformation. The contrast between Tehran–Karaj and Hashtgerd is consistent with this interpretation, although recharge, hydraulic-head evolution, aquitard geometry, and sediment compressibility were not measured jointly in the present study. The main methodological contribution is therefore the explicit separation of three questions that are often conflated in subsidence studies: whether deformation differs among land-use environments, whether recorded pumping capacity is spatially coincident with deformation intensity, and whether year-to-year pumping variation predicts deformation at a reproducible lag. Treating these questions separately, while accounting explicitly for spatial autocorrelation, yields a more defensible basis for interpretation than reliance on dense pixel-level significance or spatial co-location alone. From a management perspective, the findings support monitoring and prioritization strategies that integrate observed deformation with groundwater conditions and hydrogeological susceptibility rather than ranking areas solely by recorded well discharge or land-cover class. Hashtgerd merits particularly close investigation because strong long-term deformation occurs despite a smaller recorded pumping capacity than Tehran–Karaj, but the present results do not establish a greater deformation response per unit of abstraction. Similarly, agricultural groundwater-use zones provide a useful monitoring layer but should not be treated as deterministic predictors of annual subsidence. The severity zonation is best used as a deformation-screening product rather than a complete risk map, because exposure and vulnerability were not modeled. Future process-based assessment should combine ascending and descending InSAR or independent geodetic observations with continuous piezometry, measured abstraction and pumping duration, detailed aquifer stratigraphy, and sediment-compressibility information. Such integration would allow the spatial associations identified here to be tested against the hydraulic and geomechanical mechanisms responsible for aquifer-system compaction.

Acknowledgment

The authors gratefully acknowledge the Alborz Regional Water Company for providing access to the groundwater pumping-well records and hydrogeological technical reports used in this study, and the Alborz Plan and Budget Organization for providing provincial demographic and planning data. The authors also thank the editor and the anonymous reviewers for their constructive comments and suggestions on the manuscript.

Funding

This research received no specific grant from any funding agency in the public, commercial, or not-for-profit sectors.

Conflict of Interest

The authors declare that they have no known competing financial interests or personal relationships that could have appeared to influence the work reported in this paper.

Abbreviations

1-Small Baseline Subset (SBAS)
2-Interferometric Synthetic Aperture Radar (InSAR)
3-Persistent Scatterer Interferometry (PSI)
4-Line of Sight (LOS)
5-Land Use/Land Cover (LULC)
6-Google Earth Engine (GEE)
7-Digital Elevation Model (DEM)
8-Differential Interferometric Synthetic Aperture Radar (DInSAR)
9-Shuttle Radar Topography Mission (SRTM)
10-Topographic Position Index (TPI)
11-Normalized Difference Vegetation Index (NDVI)
12-Modified Normalized Difference Water Index (MNDWI)
13-Normalized Difference Built-Up Index (NDBI)
14-Bare Soil Index (BSI)
15-Enhanced Vegetation Index (EVI)
16-Normalized Difference Red-Edge Index (NDRE)
17-Overall Accuracy (OA)
18-Producer’s Accuracy (PA) and User’s Accuracy (UA)
19-Singular Value Decomposition (SVD)
20-Global Navigation Satellite System (GNSS)
21-Weighted Overlay Index–Best–Worst Method (WOI–BWM)
22-Thematic Mapper (TM)
23-Operational Land Imager (OLI)
24-Ground Range Detected (GRD)
25-Surface Reflectance (SR)
26-Universal Transverse Mercator (UTM)
27-World Geodetic System 1984 (WGS 84)

References

Agha alikhani, M., Karam, A., Shayan, S. and Akbary, M., 2021. Prediction of changes in morpho-climatic areas based on climate change scenarios, Alborz Province, Iran. Quantitative Geomorphological Research, v. 10(2), p. 229-247. https://doi.org/10.22034/gmpj.2021.241205.1193

Alborz Plan and Budget Organization. 2024. Deputy of Statistics and Information, [In Persian]. A. P. a. B. Organization.

Asghari Saraskanrood, S., Esfandyari Darabad, F., Faal Nazari, M. and Zeinali, B., 2025. Comparative comparison of the performance of CODAS, MABAC algorithms in zoning the risk of land subsidence using environmental indicators (case study: the boundaries of the cities of Alborz province) [In Persian]. Quantitative Geomorphological Researches, v. 13(4), p. 58-81. https://doi.org/10.22034/gmpj.2024.458189.1504

Berardino, P., Fornaro, G., Lanari, R. and Sansosti, E., 2002. A new algorithm for surface deformation monitoring based on small baseline differential SAR interferograms. IEEE Transactions on Geoscience and Remote Sensing, v. 40(11), p. 2375-2383. https://doi.org/10.1109/TGRS.2002.803792

Breiman, L., 2001. Random Forests. Machine Learning, v. 45, p. 5-32. https://doi.org/10.1023/A:1010933404324

Cohen, J., 1960. A coefficient of agreement for nominal scales. Educational and Psychological Measurement, v. 20(1), p. 37-46. https://doi.org/10.1177/001316446002000104

Delegido, J., Verrelst, J., Alonso, L. and Moreno, J., 2011. Evaluation of Sentinel-2 red-edge bands for empirical estimation of green LAI and chlorophyll content. Sensors, v. 11(7), p. 7063-7081. https://doi.org/10.3390/s110707063

Ferretti, A., Prati, C. and Rocca, F., 2001. Permanent scatterers in SAR interferometry. IEEE Transactions on Geoscience and Remote Sensing, v. 39(1), p. 8-20. https://doi.org/10.1109/36.898661

Galloway, D.L., Jones, D.R. and Ingebritsen, S.E., 1999. Land Subsidence in the United States (Circular 1182). U. S. G. Survey.

Ghanbari, A., Nakhaee, M., Kalani, S. and Azizi, H., 2026. A field-based investigation of land subsidence indicators in Alborz province, (In Persian). Journal of Engineering Geology, v. 20(1), p. 48-67. https://doi.org/10.22034/JEG.2026.20.1.10396

Goorabi, A., Karimi, M. and Allahveisi, A., 2025. Multitemporal Land Use and Land Cover Change Detection via Foundation Model Embeddings (AlphaEarth): A Pixel-Wise Similarity Framework in a Rapidly Urbanizing Semi-Arid Region (Alborz, Iran 2017–2024), (In Persian). Quantitative Geomorphological Research, v. 14(3), p. 124-149. https://doi.org/10.22034/gmpj.2026.566714.1594

Hasan, M.F., Smith, R., Vajedian, S., Pommerenke, R. and Majumdar, S., 2023. Global land subsidence mapping reveals widespread loss of aquifer storage capacity. Nature Communications, v. 14(1), 6192. https://doi.org/10.1038/s41467-023-41933-z

Huete, A., Didan, K., Miura, T., Rodriguez, E.P., Gao, X. and Ferreira, L.G., 2002. Overview of the radiometric and biophysical performance of the MODIS vegetation indices. Remote Sensing of Environment, v. 83(1-2), p. 195-213. https://doi.org/10.1016/S0034-4257(02)00096-2

Jenks, G.F., 1967. The data model concept in statistical mapping. International Yearbook of Cartography, v. 7, p. 186-190.

Kalantarian, F., Navvar Noveiri, M. and Sheikh, M., 2025. Geological and Hydrogeological Analysis of Land Subsidence in Hashtgerd Plain and Factors Affecting its Aggravation or Mitigation (In Persian). Quaternary Journal of Iran, v. 10(3-4), p. 283-296. https://doi.org/10.22034/irqua.2025.2054321.1041

Kruskal, W.H. and Wallis, W.A., 1952. Use of ranks in one-criterion variance analysis. Journal of the American Statistical Association, v. 47(260), p. 583-621. https://doi.org/10.1080/01621459.1952.10483441

Liu, Z., Ng, A.H.M., Wang, H., Chen, J., Du, Z. and Ge, L., 2023. Land subsidence modeling and assessment in the West Pearl River Delta from combined InSAR time series, land use and geological data. International Journal of Applied Earth Observation and Geoinformation, v. 118, 103228. https://doi.org/10.1016/j.jag.2023.103228

Mehrnoor, S., Robati, M., Kheirkhah Zarkesh, M.M., Farsad, F. and Baikpour, S., 2023. Land Subsidence Hazard Zoning in Hashtgerd Plain based on Integrated Multi-Criteria Decision-Making Approach: WOI-BWM. Journal of Geography and Environmental Hazards, v. 11(4), p. 127-148. https://doi.org/10.22067/geoeh.2022.75445.1188

Nakhaei, M., Mohebbi Tafreshi, A. and Saadi, T., 2023. Assessment and spatio-temporal zoning of groundwater drought risk in Hashtgerd aquifer by groundwater resource index, [In Persian]. Journal of Engineering Geology, v. 17(4), p. 444-464. https://doi.org/10.22034/JEG.2023.17.4.1019771

Noori, R., Maghrebi, M., Mirchi, A., Tang, Q., Bhattarai, R., Sadegh, M., Noury, M., Torabi Haghighi, A., Kløve, B. and Madani, K., 2021. Anthropogenic depletion of Iran's aquifers. Proceedings of the National Academy of Sciences, v. 118(25), e2024221118. https://doi.org/10.1073/pnas.2024221118

Norouzi, R., Eftekhari, S.M., Ahmadabadi, A. and Alinoori, K., 2025. Subsidence of Critical

Prohibited Well Drilling Plains (Study Area: Eshtehard Plain), [In Persian]. Journal of Applied Research in Geographical Sciences, v. 25(78), p. 66-89. https://doi.org/10.61186/jgs.25.78.24

Payne, J.A., Watson, A.R., Maghsoudi, Y., Ebmeier, S.K., Rigby, R., Lazecký, M., Thomas, M. and Elliott, J.R., 2025. Widespread Extent of Irrecoverable Aquifer Depletion Revealed by Country-Wide Analysis of Land Surface Subsidence Hazard in Iran. Journal of Geophysical Research: Solid Earth, v. 130(9), e2024JB030367. https://doi.org/10.1029/2024jb030367

Rikimaru, A., Roy, P.S. and Miyatake, S., 2002. Tropical forest cover density mapping. Tropical Ecology, v. 43(1), p. 39-47.

Rostami, A., Entezari, M. and Zakerinejad, R., 2023. Assessment and analysis of subsidence risk in Hashtgerd Plain (In Persian). Quantitative Geomorphological Research, v. 12(3), p. 140-156. https://doi.org/10.22034/gmpj.2023.414731.1454

Roy, D.P., Wulder, M.A., Loveland, T.R., Woodcock, C.E., Allen, R.G., Anderson, M.C., Helder, D., Irons, J.R., Johnson, D.M., Kennedy, R., Scambos, T.A., Schaaf, C.B., Schott, J.R., Sheng, Y., Vermote, E.F., Belward, A. S., Bindschadler, R., Cohen, W.B., Gao, F. and Zhu, Z., 2014. Landsat-8: Science and product vision for terrestrial global change research. Remote Sensing of Environment, v. 145, p. 154-172. https://doi.org/10.1016/j.rse.2014.02.001

Safdari, Z., Nahavandchi, H. and Joodaki, G., 2022. Estimation of Groundwater Depletion in Iran's Catchments Using Well Data. Water, v. 14(1), 131 p. https://doi.org/10.3390/w14010131

Shiri, M., Lashkaripour, G.R. and Hafezi Moghadas, N., 2024. Integrated AHP and DInSAR Approach for Land Subsidence Hazard Assessment in Karaj Plain, Iran. Geopersia, v. 14(2), p. 397-418. https://doi.org/10.22059/geope.2024.374588.648751

Terzaghi, K., 1943. Theoretical Soil Mechanics. John Wiley & Sons.

Torres, R., Snoeij, P., Geudtner, D., Bibby, D., Davidson, M., Attema, E., Potin, P., Rommen, B., Floury, N., Brown, M., Traver, I.N., Deghaye, P., Duesmann, B., Rosich, B., Miranda, N., Bruno, C., L'Abbate, M., Croci, R., Pietropaolo, A. and Rostan, F., 2012. GMES Sentinel-1 mission. Remote Sensing of Environment, v. 120, p. 9-24. https://doi.org/10.1016/j.rse.2011.05.028

Tucker, C.J., 1979. Red and photographic infrared linear combinations for monitoring vegetation. Remote Sensing of Environment, v. 8(2), p. 127-150. https://doi.org/10.1016/0034-4257(79)90013-0

Xu, H., 2006. Modification of Normalized Difference Water Index (NDWI) to Enhance Open Water Features in Remotely Sensed Imagery. International Journal of Remote Sensing, v. 27(14), p. 3025-3033. https://doi.org/10.1080/01431160600589179

Zha, Y., Gao, J. and Ni, S., 2003. Use of Normalized Difference Built-Up Index in Automatically Mapping Urban Areas from TM Imagery. International Journal of Remote Sensing, v. 24(3), p. 583-594. https://doi.org/10.1080/01431160304987

Zhao, F., Miao, F., Wu, Y., Xiong, Y., Gong, S. and Sun, D., 2024. Land subsidence susceptibility mapping in urban settlements using time-series PS-InSAR and random forest model. Gondwana Research, v. 125, p. 406-424. https://doi.org/10.1016/j.gr.2023.09.019